AD-A141 551 INVESTIGATION OF THE MECHANISM OF TRANSONIC SHOCK 1/1
WAVE/BOUNDARY LAYER INT..(U) SCIENTIFIC RESEARCH
ASSOCIATES INC GLASTONBURY CT D V ROSCOE ET AL. MAY 84
UNCLASSIFIED SRA-RB3-930006-F ARO-17048.1-EG F/G 20/4 NL

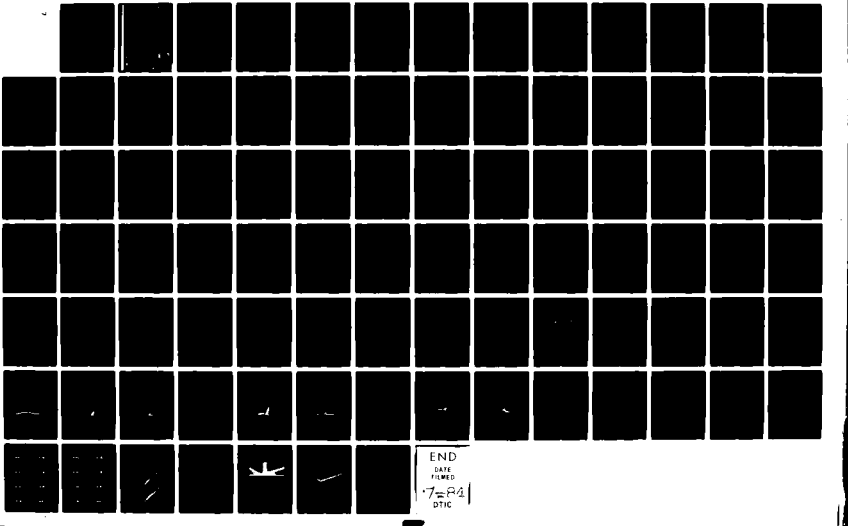

END
DATE FILMED
7-84
DTIC

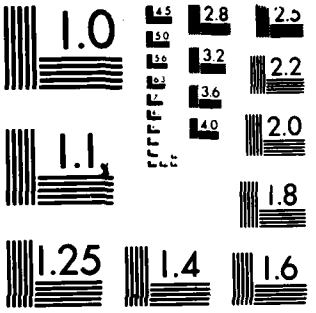

# INVESTIGATION OF THE MECHANISM OF TRANSONIC SHOCK WAVE/BOUNDARY LAYER INTERACTIONS USING A NAVIER-STOKES ANALYSIS

(FINAL REPORT)

D.V. Roscoe
S.J. Shamroth
H.J. Gibeling
H. McDonald

May 1984

U.S. ARMY RESEARCH OFFICE
Contract DAAG29-80-C-0082

Prepared by

SCIENTIFIC RESEARCH ASSOCIATES, INC.
P.O. Box 498
Glastonbury, CT 06033

UNCLASSIFIED

SECURITY CLASSIFICATION OF THIS PAGE (When Data Entered)

| REPORT DOCUMENTATION PAGE | | READ INSTRUCTIONS BEFORE COMPLETING FORM |
|---|---|---|
| 1. REPORT NUMBER | 2. GOVT ACCESSION NO. N/A | 3. RECIPIENT'S CATALOG NUMBER N/A |
| 4. TITLE (and Subtitle) Investigation of the Mechanism of Transonic Shockwave/Boundary Layer Interactions Using a Navier-Stokes Analysis | | 5. TYPE OF REPORT & PERIOD COVERED Final Report July 1980 - May 1983 |
| | | 6. PERFORMING ORG. REPORT NUMBER SRA Report R83-930006-F |
| 7. AUTHOR(s) D. V. Roscoe, S. J. Shamroth, H. J. Gibeling, H. McDonald | | 8. CONTRACT OR GRANT NUMBER(s) DAAG29-80-C-0082 |
| 9. PERFORMING ORGANIZATION NAME AND ADDRESS Scientific Research Associates, Inc. P.O. Box 498 100 Sycamore Street Glastonbury, CT 06033 | | 10. PROGRAM ELEMENT, PROJECT, TASK AREA & WORK UNIT NUMBERS |
| 11. CONTROLLING OFFICE NAME AND ADDRESS U. S. Army Research Office Post Office Box 12211 Research Triangle Park, NC 27709 | | 12. REPORT DATE May 1984 |
| | | 13. NUMBER OF PAGES |
| 14. MONITORING AGENCY NAME & ADDRESS(if different from Controlling Office) | | 15. SECURITY CLASS. (of this report) Unclassified |
| | | 15a. DECLASSIFICATION/DOWNGRADING SCHEDULE |

16. DISTRIBUTION STATEMENT (of this Report)

Approved for public release; distribution unlimited.

17. DISTRIBUTION STATEMENT (of the abstract entered in Block 20, if different from Report)

NA

18. SUPPLEMENTARY NOTES

The view, opinions, and/or findings contained in this report are those of the author(s) and should not be construed as an official Department of the Army position, policy, or decision, unless so designated by other documentation.

19. KEY WORDS (Continue on reverse side if necessary and identify by block number)

Multidimensional Implicit, Time Marching, Navier-Stokes, Shock Wave/Boundary Layer Interaction, Adaptive Grid, Transonic Bump Flow, Impinging Shock, Normal Shock

20. ABSTRACT (Continue on reverse side if necessary and identify by block number)

The present report discusses the development of a time-dependent Navier-Stokes code for use in predicting transonic shock-wave boundary layer interaction. In addition, various test cases which have been performed are discussed. The algorithm used to solve the equations is based upon the consistently split linearized block implicit method of Briley and McDonald [15, 16]. The philosophy and use of a solution adaptive mesh is also described. The test cases studied in this report are: normal shock wave boundary layer interaction in a constant → cont'd

DD FORM 1 JAN 73 1473 EDITION OF 1 NOV 65 IS OBSOLETE

UNCLASSIFIED

SECURITY CLASSIFICATION OF THIS PAGE (When Data Entered)

area circular pipe, steady transonic flow over an axisymmetric bump, unsteady flow over an axisymmetric bump, supersonic flow over an axisymmetric compression corner and oblique shock wave impingement on a flat plate boundary layer.

## LIST OF SYMBOLS

Symbols

| | |
|---|---|
| $A^+$ | van Driest damping coefficient |
| $C_p$ | specific heat at constant pressure |
| $D$ | determinant of the Jacobian matrix |
| $\Phi$ | dissipation function |
| $d$ | distance to the nearest wall |
| $d^+$ | dimensionless distance to the nearest wall |
| $h$ | enthalpy, throat height |
| $\ell$ | mixing length |
| $\ell_\infty$ | mixing length in the core flow region |
| $p$ | static pressure |
| $q$ | magnitude of the velocity |
| $\vec{q}_T$ | turbulent heat flux vector |
| $\vec{\bar{q}}$ | mean heat flux vector |
| $R$ | universal gas constant |
| $R_e$ | Reynolds number |
| $t$ | time |
| $T$ | temperature |
| $T^\circ$ | stagnation temperature |
| $\vec{u}$ | velocity vector |
| $u$ | velocity component in x-direction |
| $u_\tau$ | friction velocity |
| $v$ | velocity component in y-direction |

LIST OF SYMBOLS (Continued)

Symbols

| | |
|---|---|
| $w$ | velocity component in z-direction |
| $w_e$ | w at the edge of the boundary layer |
| $x$, $x_1$ | cartesian coordinate in transverse direction |
| $y$, $y_2$ | cartesian coordinate in spanwise direction |
| $y^1$, $y^2$, $y^3$ | computational coordinates |
| $z$, $x_3$ | cartesian coordinate in streamwise direction |

Greek Symbols

| | |
|---|---|
| $\delta$ | boundary layer thickness |
| $\varepsilon$ | turbulence energy dissipation rate |
| $\kappa$ | von Karman constant |
| $\mu$ | dynamic viscosity |
| $\nu_{art}$ | artificial dissipation |
| $\xi$, $\eta$, $\zeta$ | computational coordinates |
| $\bar{\bar{\pi}}$ | molecular stress tensor |
| $\pi^T$ | turbulent stress tensor |
| $\rho$ | density |
| $\sigma$ | artificial dissipation parameter |
| $\tau$ | time |
| $\tau_\ell$ | local shear stress |
| $\tau_{xx}$, $\tau_{xy}$, etc. | component of stress tensor |
| $\phi$ | meanflow dissipation rate |

Subscripts

| | |
|---|---|
| b | associated with the bottom wall |
| s | associated with the side wall |
| t | associated with the time or top wall |
| x | associated with the x-direction |
| y | associated with the y-direction |
| z | associated with the z-direction |

Superscripts

| | |
|---|---|
| T | associated with turbulent quantities, transpose of matrix |

TABLE OF CONTENTS

# INTRODUCTION

The flow field resulting from the interaction of a shock wave and a boundary layer on a projectile or missile remains a major problem which has yet to be completely analyzed. The interaction process plays an important role in several areas. Among these are: (i) body lift and drag, (ii) side force development and control and (iii) heat transfer. Since the interaction causes an abrupt pressure rise and boundary layer thickening and may be accompanied by regions of local separation, the interaction flow can be a major contributor to the overall body drag and can cause substantial changes from the potential flow pressure distribution. Furthermore, since the interactions are often three-dimensional due to either geometric or flow incidence effects, the generated forces may not be symmetric and may result in sigificant side forces. These side forces, in turn, can lead to serious control and guidance problems. Finally, the shock wave boundary layer interaction zone may be a region of severe heat transfer. The problems associated with interactions are particularly troublesome at transonic speeds where both the shock location and its shape are very sensitive to minor changes in flow geometry. As a consequence, in recent years there has been considerable interest in the development of accurate and efficient prediction techniques for this category of the interaction problem.

At present, two main approaches for treating the shock wave-boundary layer interaction problem are being pursued. The first termed the strong interaction approach divides the flow region of interest into two parts, an outer inviscid part and a wall viscous part. Each region is then solved separately via the appropriate set of equations for that region. Equations appropriate for inviscid flows; e.g., Euler, potential flow or simple wave relations, are used in the outer region and boundary layer equations are used in the inner region. At the juncture of the regions, matching conditions which require continuity of all flow variables are applied. In flow situations in which the outer flow is supersonic and thus described by hyperbolic equations, a solution can be forward-marched in space with the inviscid and viscous regions coupled on a station-by-station basis. The chief difficulty in this process is that mathematically stiff equations must be solved. Common problems with stiff equations manifest themselves in the form of numerical solutions which can branch off the desired solution thus producing a

physically unrealistic result. In regions where the inviscid flow is subsonic and thus described by elliptic equations, a forward-marching procedure without iteration is not physically realistic since the upstream pressure propagation is not modeled. Consequently a sequence of inviscid and boundary layer solutions must be performed in a manner in which each stage corrects the former stage through global iteration. Additional problems occur in transonic flows where both supersonic and subsonic outer regions are present and where small displacement effects may have considerable influence on shock location and overall pressure distribution. In cases where the nominally inviscid flow is subsonic behind the shock the situation is further complicated by the subsonic outer region being elliptic. Since the flow cannot be forward marched here, a global rather than a station-by-station iteration must be used.

If an iteration procedure is to be used, the viscous layer can be solved iteratively by either a forward-marching boundary layer calculation procedure or as the asymptotic condition of a time or pseudo-time dependent integration. In the case of steady state forward-marching boundary layer procedures, problems are encountered when the boundary layer is subjected to an adverse pressure gradient strong enough to cause separation. Although a boundary layer procedure can be forward marched through separation by suppressing streamwise convection terms in the separated flow region, via the so called FLARE approximation [1], the resulting solution is based upon an approximation made in the separated flow region which becomes progressively more inaccurate as the backflow velocities increase. Therefore, calculated details of the flow in this region cannot be expected to be accurate with significant backflow using FLARE. A global, but time consuming, iteration [2] is necessary to replace the FLARE approximation, and at this point the efficiency of the forward-marching scheme must be carefully evaluated to ensure a net gain exists relative to solving the full Navier-Stokes equations for the viscous layer. Time integration of the interaction between the boundary layer and the external flow can be structured to avoid the use of either FLARE or the global iteration to account specifically for the backflow velocity [2], and in some cases the time marched iteration approach may show a significant gain relative to solving the Navier-Stokes equations for the viscous flow region. However, the interaction approach remains limited, even with time integration, to

flows where the division of the flow into zones which can be interacted is reasonable and details of any separated zone are not of major interest. A discussion of some of the early techniques aimed at the shock wave-boundary layer interaction problem which are based upon a viscous-inviscid approach is given by Hankey [3].

The second approach used in obtaining solutions for shock wave-boundary layer flow field is the fully viscous analysis. The fully viscous analysis solves the entire flow field via a single set of equations, thus avoiding any need to divide the flow into viscous and inviscid regions. The Navier-Stokes analyses pursued to date include explicit, implicit and hybrid numerical formulations. For example, in a very early work of this type, MacCormack [4] applied an explicit procedure to the laminar interaction problem. In subsequent work MacCormack and his co-workers have used this explicit method extensively in analyzing the interaction flow field [5-8]. The basic method has also been used by Shang and Hankey [9] in calculating turbulent flow over a compression ramp and in predicting a streamwise corner interaction region [10]. Recently MacCormack has developed a new hybrid explicit-implicit characteristics method [11] which is considerably faster than the fully explicit method [4-10], and has applied this technique to shock wave-boundary layer interaction problems. This same technique has also been applied to axisymmetric interaction flow fields by Viegas and Coakley [12].

In addition to the fully explicit investigations of Ref. 4-10, and the hybrid investigations of Refs. 11 and 12, Levy, Shamroth, Gibeling and McDonald [13] and Beam and Warming [14] have applied implicit solution procedures to the interaction flow field problem. In the former investigation, Levy et al applied the Briley-McDonald consistently split Linearized Block Implicit (LBI) solution procedure [15, 16] to the shock wave-boundary layer interaction problem in a feasibility study which was part of a larger effort primarily focused on a boundary layer strong interaction study. Beam and Warming [14] also applied a similar implicit scheme to the interaction problem.

To date many investigations have focused upon the interaction flow field problem. Most of the analyses have concentrated upon two specific problems; (i) flat plate - ramp compression corners and (ii) two-dimensional shock impingement on a flat plate. The problem of axisymmetric transonic interactions which may be particularly relevant in missile or projectile

applications has received less attention. Prior to the present study, Viegas and Coakley [12] applied MacCormack's hybrid technique to an interaction occurring on an axisymmetric body. Little other work has concentrated upon the axisymmetric problem.

This report presents and describes the development and application of a fully viscous method for solving transonic shock wave-boundary layer interaction problems. The method utilizes the Briley and McDonald [15, 16] linearized block implicit (LBI) technique for the numerical solution of the multidimensional, time-dependent Navier-Stokes equations, and has been applied to several axisymmetric flow problems. These include transonic flow in a constant area axisymmetric pipe, transonic flow over an axisymmetric bump, shock inducement at an axisymmetric compression corner and the two-dimensional flat plate boundary layer - impinging shock wave interaction problem. In addition to these steady flow cases, several time-dependent problems are reported in which the transonic flow over an axisymmetric bump was subjected to downstream static pressure oscillation.

In the following sections, the governing equations are presented and a general description of their transformation to general curvilinear coordinates is given. However, description of the specific coordinate transformation used for each case is presented on a case-by-case basis.

## ANALYSIS

### Governing Equations

The equations used in the present effort are the ensemble-averaged, time-dependent Navier-Stokes equations which can be written in vector form as

Continuity

$$\frac{\partial \rho}{\partial t} + \nabla \cdot \rho \vec{u} = 0 \tag{1}$$

Momentum

$$\frac{\partial \rho \vec{u}}{\partial t} + \nabla \cdot (\rho \vec{u}\vec{u}) = - \nabla p + \nabla \cdot (\bar{\bar{\pi}} + \pi^T) \tag{2}$$

Energy

$$\frac{\partial \rho h}{\partial t} + \nabla \cdot (\rho \vec{u} h) = - \nabla \cdot (\vec{q} + \vec{q}^{T}) + \frac{Dp}{Dt} + \Phi + \rho\varepsilon \qquad (3)$$

where $\rho$ is density, u is velocity, p is pressure, $\pi$ is the molecular stress tensor $\pi^T$ is the turbulent stress tensor, h is enthalpy, q is the mean heat flux vector, $q^T$ is the turbulent heat flux vector, $\Phi$ is the mean flow dissipation rate and $\varepsilon$ is the turbulence energy dissipation rate. If the flow is assumed at a constant total temperature, the energy equation is replaced by

$$T_o = T + \frac{q^2}{2C_p} = \text{constant} \qquad (4)$$

where $T_o$ is the stagnation temperature, q is the magnitude of the velocity and $C_p$ is the specific heat at constant pressure. In a number of cases considered in this work the assumption of constant total temperature has been invoked by using Eq. 4 as an approximation to Eq. 3 for the sole purpose of reducing computer run time where the constant $T_o$ assumption was warranted. Cases in which this substitution has been made are identified in the text describing results. A number of terms appearing in Eqs. 1-4 require definition. The stress tensor appearing in Eq. 2 is defined as

$$\pi = 2\mu\mathbb{D} - \left(\frac{2}{3}\mu - K_B\right) \nabla \cdot \vec{U}\, \Pi \qquad (5)$$

where $K_B$ is the bulk viscosity coefficient and  is the deformation tensor, defined by:

$$\mathbb{D} \equiv \frac{1}{2}\left((\nabla\vec{U}) + (\nabla\vec{U})^T\right) \qquad (6)$$

In addition the turbulent stress tensor has been modeled using an isotropic eddy viscosity such that:

$$\pi^T = - \rho \overline{\vec{u}' \vec{u}'} = 2\mu_T \mathbb{D} \qquad (7)$$

where $\mu_T$, the turbulent viscosity, is determined by a suitable turbulence model. Turbulence modeling is described in some detail in the next section.

Equation 3 contains a mean heat flux vector defined as follows:

$$\vec{q} = - \kappa (\nabla T) \qquad (8)$$

and a turbulent heat flux vector defined as:

$$\vec{q}^{T} = -\kappa^{T} (\nabla T) \tag{9}$$

where $\kappa$ and $\kappa^T$ are the mean and turbulent thermal conductivities, respectively.

Also appearing in Eq. 3 is the mean flow dissipation term $\Phi$.

$$\Phi = 2\mu \mathbb{D} : \mathbb{D} - \left(\frac{2}{3}\mu - K_B\right) (\nabla \cdot \vec{U})^2 \tag{10}$$

The equation of state for a perfect gas

$$p = \rho RT \tag{11}$$

where R is the gas constant, the caloric equation of state

$$e = c_v T \tag{12}$$

and the definition of static enthalpy

$$h = c_p T \tag{13}$$

supplement the equations of motion.

Finally the flow properties $\mu$, $\kappa$ and $K_B$ are determined using the following constitutive relations.

The molecular viscosity $\mu$ is determined using Sutherland's law.

$$\frac{\mu}{\mu_o} = \left(\frac{T}{T_o}\right)^{3/2} \frac{T_o + S_1}{T + S_1} \tag{14}$$

where $S_1 = 100°K$ for air.

The bulk viscosity will be assumed to be zero,

$$K_B = 0 \tag{15}$$

and the thermal conductivity may be determined by use of a relation similar to Sutherland's law viz.

$$\frac{\kappa}{\kappa_o} = \left(\frac{T}{T_o}\right)^{3/2} \frac{T_o + S_2}{T + S_2} \tag{16}$$

where $S_2 = 194°K$ for air.

## Turbulence Modeling

Several alternative turbulence models have been considered in the course of the present work. In general terms, the models used were zero, one- and two-equation models. The formulation of each is described in this section.

### Zero Equation Model - (Mixing Length)

Of all available turbulence models, Prandtl's mixing length model is probably still the most widely used. The model was originally developed for use in unseparated boundary layer flow situations and has been shown to perform well under such conditions. In the cases described in this report the mixing length model has been used extensively in order to investigate its use in the shock wave/boundary layer interaction problem. An advantage of the method from the point of view of economy is that is does not require additional transport equations to model the effect of turbulence, but rather relates the Reynold's shear stress to mean flow quantities via:

$$\overline{\rho u_i' u_j'} = \frac{\mu_T}{R_e} \frac{\partial u_j}{\partial x_i}$$

where

$$\frac{\mu_T}{Re} = \rho \ell^2 (2\mathbb{D} : \mathbb{D})^{1/2}$$

where

$$\ell = \min[\ell_{,\infty} \kappa d D]$$

where d is the normal distance to the nearest wall and D is van Driest damping coefficient given by

$$\begin{aligned} D &= 1 - \exp(- y^+/A^+) \\ \ell_\infty &= 0.09\delta \\ \kappa &= 0.4 \\ y^+ &= du_\tau/\nu \\ u_\tau &= (\tau_\ell/\rho)^{1/2} \end{aligned} \tag{17}$$

where the local shear stress $\tau_\ell$ is obtained from

$$\tau_\ell = (2\mathbb{D} : \mathbb{D})^{1/2} \tag{18}$$

and $\mathbb{D}$ is defined by Eq. 6.

One problem in the mixing length formulation is the definition of $\delta$. In boundary layers the streamwise velocity u approaches an edge velocity, $u_e$, asymptotically, however, a monotonic approach to an asympototic edge velocity is not characteristic of Navier-Stokes solutions. In order to avoid the problem of determining the boundary layer edge, $\delta$, as defined in the usual boundary layer context, i.e., $\delta$ is the distance from the wall at which $u/u_e = 0.99$, the following relation is used.

$$\delta = 2.0 d_{(q/q_{max}=c)} \tag{19}$$

In other words, $\delta$, is taken as twice the distance (measured away from the nearest wall) for which $q/q_{max} = c$. The value of c used in the present effort was 0.90.

One-Equation Model - (k-$\ell$)

Although as discussed above the mixing length concept is valid for a variety of flows, some important flow situations arise in which a less restrictive model is required. One such model is the one-equation turbulence model [17, 18, 19] in which a transport equation for turbulence kinetic energy, k, is formulated as follows:

$$\frac{\partial(\rho k)}{\partial t} + \nabla\cdot(\rho\vec{U}k) = \nabla\cdot\left(\frac{\mu_T}{\sigma_k}\nabla k\right) + 2\mu_T\left(\mathbb{D}:\mathbb{D}\right) - \rho\varepsilon$$

where following Ref. 20, $\sigma_k$ is set to 1.0, and k is the turbulence kinetic energy

$$k = \frac{1}{2}\ \overrightarrow{u'\cdot u'_2} \tag{20}$$

and the Prandtl-Kolmogorov relation, Eq. 21, defines the turbulent viscosity as:

$$\mu_T = c_\mu \frac{\rho k^2}{\varepsilon} \tag{21}$$

In addition, the turbulence dissipation rate $\varepsilon$ is determined by:

$$\varepsilon = c_\mu^{3/4} \frac{k^{3/2}}{\ell} \tag{22}$$

where $\ell$, is a relevant turbulent length scale for the problem of interest. The k-$\ell$ model has an advantage over the mixing length model in that the use

of a transport equation for turbulence kinetic energy allows for its convection, production and dissipation. This is important because it allows a nonequilibrium effect on the turbulence to be included in the calculation while the mixing length model can only account for local equilibrium turbulence effects via its association with the mean velocity field. A major disadvantage which the k-$\ell$ model shares with the mixing length model is the requirement of length scale specification. Typically the mixing length, as described in the previous section, is used as the representative length scale.

In modeling the flow in the near wall region where low local turbulence Reynolds' numbers occur, two approaches are available. The first is the wall function approach which does not resolve the near wall region but assumes specific functional forms for the required turbulence quantities and uses these forms to create the required normal derivative formulations at the first grid point from the wall. Such an approach obviously requires a detailed knowledge of the turbulence model dependent variables in the vicinity of the wall. Although reasonable functional formulations can be specified for simple flows such as constant pressure boundary layers, specification in the much more complex flows of current interest are much more difficult. Therefore, the alternative approach in which the viscous sublayer is resolved has been used. The method makes no approximation at the boundary, but requires that the near wall low turbulence Reynolds' number physics be modeled. In this work, a near wall model which was successfully used by Shamroth and Gibeling [21] in a time-dependent airfoil flow field analysis, has been implemented in the computer code. The analysis of Ref. 21 follows the integral turbulence energy procedure of Refs. 22 - 24 by utilizing a turbulence function $a_1$, where

$$a_1 = \frac{1}{2} c_\mu^{1/2} \tag{23}$$

and $a_1$ is taken as a function of a turbulence Reynolds's number of the form

$$a_1 = a_o \left[\frac{f(R_\tau)}{100}\right] \Bigg/ \left[1.0 + 6.66\, a_o \left(\frac{f(R_\tau)}{100} - 1\right)\right] \tag{24}$$

$$a_o = .0115$$

$$\begin{aligned} f(R_\tau) &= 100\, R_\tau^{0.22} && R_\tau \leq 1 \\ f(R_\tau) &= 68.1\, R_\tau + 614.3 && R_\tau \geq 40 \end{aligned} \tag{25}$$

and a cubic curve was fitted for values of $R_\tau$ between 1 and 40. As previously discussed, Refs. 22 - 24 utilized an integral form of the turbulence kinetic energy and, therefore, $R_\tau$ was defined as an average value.

$$R_\tau = \frac{1}{\delta} \int_o^\delta \nu_\tau \, dy \; / \; \frac{1}{\delta} \int_o^{\delta_s} \nu \, dy_s \tag{26}$$

In the present effort $R_\tau$ was defined as the local ratio of turbulent to laminar viscosity, $a_1$ was evaluated via Eq. 24 and $C_\mu$ related to $a_1$ via Eq. 23.

Two-Equation Model - (k-ε)

Although the one-equation approach does relieve some restrictions present in the mixing length approach, it still requires specification of a length scale. The k-ε, two-equation turbulence model [20, 40] in which both the turbulence kinetic energy and the turbulence dissipation rate are governed by transport equations represents a more general model. In this approach the k-equation is as given in Eq. 20, but the algebraic relation for ε given by Eq. 22 is replaced by the following transport equation.

$$\frac{\partial}{\partial t}(\rho\bar{\varepsilon}) + \nabla\cdot(\rho\vec{u}\bar{\varepsilon}) = \nabla\cdot\left(\frac{\mu_T}{\sigma_\varepsilon}\nabla\bar{\varepsilon}\right) + c_1(2\mu_T \, \mathbb{D} : \mathbb{D}) + 2\mu\mu_T(\nabla^2 U)^2 - c_2\rho\frac{\varepsilon}{k} \tag{27}$$

where following Reference 20

$$c_1 = 1.55$$

and

$$c_2 = c_{2\infty} \; [1 - 0.3 \exp(-R_T)^2]$$

$$c_{2\infty} = 2.0$$

and $R_T$ is defined as:

$$R_T = \frac{\rho k^2}{\varepsilon\mu}$$

However, attempts to solve Eqs. 20 and 27 without modification fail because an appropriate boundary condition for ε at a solid boundary is difficult to prescribe such that Eq. 27 is satisfied. In order to circumvent this problem, Eq. 27, the turbulence dissipation equation, has been modified by the inclusion of the term:

$$- 2\mu\mu_T \, (\nabla^2 U)^2$$

which following Jones and Launder [20] is included in order to obtain better agreement with experimentally determined k distributions in the near-wall region. In addition, Jones and Launder's [20] inclusion of the term:

$$- 2\rho\nu \left(\nabla k^{1/2}\right)^2$$

in Eq. 28 is a numerical device, rather than a physical model, which allowed $\varepsilon$=0 to be prescribed as a function boundary condition [20].

$$\frac{\partial(\rho k)}{\partial t} + \nabla \cdot (\rho \vec{U} k) = \nabla \cdot \frac{\mu_T}{\sigma_k} \nabla k + 2\mu_T \left( \mathbb{D} : \mathbb{D} \right) - \rho\varepsilon - 2\rho\nu \left(\nabla k^{1/2}\right)^2 \qquad (28)$$

## COORDINATE SYSTEM DETAILS

Equations 1 - 3 and 27 - 28 are written in vector form in which the spatial dependent variables represent a general curvilinear system $y^j$ ($j = 1, 2, 3$). In principle an arbitrary coordinate system can be used, however experience has shown that to obtain accurate and economical numerical solutions the coordinate system used must meet certain criteria. These include the ability to permit accurate implementation of boundary conditions, sufficient smoothness of coordinate data and flexible distribution of computational grid points. The first factor to be considered concerns the treatment of boundary conditions. The specification of boundary conditions which do not fall upon coordinate lines or at specific grid points can present a difficult problem for numerical analyses. Although finite difference molecules can be constructed for boundary points which do not fall upon coordinate lines, such molecules may have an unacceptably high spatial truncation error associated with them. It should be noted that while the boundary condition problem arises in both viscous and inviscid analyses, it is considerably more severe in viscous flows where no-slip conditions on solid walls can combine with boundary condition truncation error to produce numerical solutions which are both qualitatively and quantitatively in error. Thus, the first property required of any coordinate system to be used in a viscous analysis should be that boundary surfaces coincide with coordinate surfaces. A second coordinate system requirement is sufficient smoothness of geometric data. This requirement is more stringent than simply requiring the existence of a given number of analytically determined coordinate transformation derivatives; the coordinates must not have large changes in the coordinate geometry metric data between grid points. Such large changes can cause serious deterioration of solution accuracy or even prevent obtaining a converged solution. The final item to be considered is the need to obtain high grid resolution in specified regions of the flow field. For example, the wall region of viscous flows is characterized by rapid changes in flow variables, therefore the computational grid should have a distribution of points designed to resolve these gradients. In other regions the flow variables change slowly and these regions should have a relatively sparse computational grid associated with them, in order to maintain an economic solution.

A recent review of grid generation techniques has been made by Thompson [25] who presents an extensive overview of available grid generation techniques. In summary, these include the elliptic methods popularized by Thompson et al [26], the conformal techniques typified by Moretti's work [27], and the constructive approach such as that of Eiseman [28].

The governing equations for the present problems have been given in the previous section in vector form (Eqs. 1 - 3 and 27 - 28). However, implementation of a solution procedure requires that these equations be transformed into an appropriate coordinate system. Therefore, the governing equations written in a cylindrical-polar coordinate system are transformed with a general Jacobian transformation of the form

$$\begin{aligned} y^j &= y^j(\bar{x}_1, \bar{x}_2, \bar{x}_3, t) \\ \tau &= t \end{aligned} \tag{29}$$

where $(\bar{x}_1, \bar{x}_2, \bar{x}_3) = (r, \theta, z)$ are the original cylindrical polar coordinates. The velocity components remain the components $(U_1, U_2, U_3)$ in the $(\bar{x}_1, \bar{x}_2, \bar{x}_3)$ coordinate directions, respectively. The new independent variables $y^j$ are the computational coordinates in the transformed system. The coordinate system requirements for the current application may be represented by a subset of the general transformation, Eq. 29,

$$y^1 = y^1(\bar{x}_1, \bar{x}_3, t) \qquad (a)$$

$$y^2 = y^2(\bar{x}_2) \qquad (b) \tag{30}$$

$$y^3 = y^3(\bar{x}_1, \bar{x}_3, t) \qquad (c)$$

which is a general axisymmetric time-dependent-transformation. For axisymmetric flows, Eq. 30b reduces to $y^2 = \bar{x}_2$, and all derivatives $\partial/\partial y^2$ are assumed to be zero. The transformation, Eq. 30, with the axisymmetric flow assumption has been utilized in the computer code developed under the present effort.

Application of the Jacobian transformation requires expansion of the temporal and spacial derivatives using the chain rule, i.e.,

$$\frac{\partial \phi}{\partial t} = \frac{\partial \phi}{\partial \tau} + \sum_{j=1}^{3} y^j_{,t} \frac{\partial \phi}{\partial y^j} \tag{31}$$

and

$$\frac{\partial \phi}{\partial \bar{x}_i} = \sum_{j=1}^{3} y^j{}_{,i} \frac{\partial \phi}{\partial y^j} \tag{32}$$

where

$$y^j{}_{,t} \equiv \frac{\partial y^j}{\partial t}$$

$$y^j{}_{,i} \equiv \frac{\partial y^j}{\partial \bar{x}_i} \tag{33}$$

The relations Eqs. 32 - 33 are first substituted into the governing equations written in cylindrical polar coordinates. Then the resulting equations are multiplied by the Jacobian determinant of the inverse transformation,

$$J = \frac{\partial(\bar{x}_1, \bar{x}_2, \bar{x}_3)}{\partial(y^1, y^2, y^3)} = \begin{vmatrix} \frac{\partial \bar{x}_1}{\partial y^1} & \frac{\partial \bar{x}_1}{\partial y^2} & \frac{\partial \bar{x}_1}{\partial y^3} \\ \frac{\partial \bar{x}_2}{\partial y^1} & \frac{\partial \bar{x}_2}{\partial y^2} & \frac{\partial \bar{x}_2}{\partial y^3} \\ \frac{\partial \bar{x}_3}{\partial y^1} & \frac{\partial \bar{x}_3}{\partial y^2} & \frac{\partial \bar{x}_3}{\partial y^3} \end{vmatrix} \tag{34}$$

and the equations are cast into a conservative form using the following relations

$$\sum_{j=1}^{3} \frac{\partial \tilde{y}^j{}_{,i}}{\partial y^j} = 0 \tag{35}$$

$$\frac{\partial J}{\partial \tau} + \sum_{j=1}^{3} \frac{\partial \tilde{y}^j{}_{,t}}{\partial y^j} = 0 \tag{36}$$

where

$$\tilde{y}^j{}_{,i} \equiv J y^j{}_{,i}$$

$$\tilde{y}^j{}_{,t} \equiv J y^j{}_{,t} \tag{37}$$

It should be noted that Equation 36 expresses a geometric conservation law and plays an important role in enabling the equations of motion to be cast into conservative form.

The particular conservation form developed implies that all factors involving the radial coordinate $r = \bar{x}_1$ remain as they were before the Jacobian transformation. The resulting equations are presented below as Eqs. 40 - 49.

The geometric relations Eq. 35 - 36 may be obtained from the transformation relations for $\ddot{y}^j_{,t}$ and $\ddot{y}^j_{,i}$ in terms of the inverse transformation derivatives (e.g., Reference 29),

$$
\begin{aligned}
\ddot{y}^1{}_{,1} &= \bar{x}_{2,2}\,\bar{x}_{3,3} - \bar{x}_{2,3}\bar{x}_{3,2} \\
\ddot{y}^1{}_{,2} &= \bar{x}_{3,2}\,\bar{x}_{1,3} - \bar{x}_{3,3}\,\bar{x}_{1,2} \\
\ddot{y}^1{}_{,3} &= \bar{x}_{1,2}\,\bar{x}_{2,3} - \bar{x}_{1,3}\,\bar{x}_{2,2} \\
\ddot{y}^2{}_{,} &= \bar{x}_{2,3}\,\bar{x}_{3,1} - \bar{x}_{2,1}\,\bar{x}_{3,3} \\
\ddot{y}^2{}_{,2}{}^1 &= \bar{x}_{3,3}\,\bar{x}_{1,1} - \bar{x}_{3,1}\,\bar{x}_{1,3} \\
\ddot{y}^2{}_{,3} &= \bar{x}_{1,3}\,\bar{x}_{2,1} - \bar{x}_{1,1}\,\bar{x}_{2,3} \\
\ddot{y}^3{}_{,1} &= \bar{x}_{2,1}\,\bar{x}_{3,2} - \bar{x}_{2,2}\,\bar{x}_{3,1} \\
\ddot{y}^3{}_{,2} &= \bar{x}_{3,1}\,\bar{x}_{1,2} - \bar{x}_{3,2}\,\bar{x}_{1,1} \\
\ddot{y}^3{}_{,3} &= \bar{x}_{1,1}\,\bar{x}_{2,2} - \bar{x}_{1,2}\,\bar{x}_{2,1}
\end{aligned}
\tag{38}
$$

$$
\ddot{y}^j{}_{,t} = -\sum_{k=1}^{3} \ddot{y}^j{}_{,k}\,\frac{\partial \bar{x}_k}{\partial \tau} \tag{39}
$$

The transformed governing equations may be written in the following compact form:

$$
\begin{aligned}
\frac{\partial (J\vec{W})}{\partial \tau} = &-\sum_{j=1}^{3} \frac{\partial}{\partial y^j}\,(Jy^j{}_{,t}\vec{W}) - \sum_{j=1}^{3} \Big[\beta_i \frac{\partial}{\partial y^j}\,(Jy^j{}_{,i}\vec{F}_i) \\
&+ \gamma_i \frac{\partial}{\partial y^j}(Jy^j{}_{,i}\,\vec{P}_i) + \zeta_i \frac{\partial}{\partial y^j}\,(Jy^j{}_{,i}\,\vec{G}_i)\Big] \\
&+ J\vec{S} + J\vec{C}
\end{aligned}
\tag{40}
$$

where

$$y,^{j}_{t} \equiv \frac{\partial y^{j}}{\partial t}$$
$$y,^{j}_{i} \equiv \frac{\partial y^{j}}{\partial \bar{x}_{i}} \tag{41}$$

Further, the coefficients $\beta_i$, $\gamma_i$, $\zeta_i$ are given by

$$\begin{aligned} \beta_1 &= \frac{1}{r}, \quad \beta_2 = \frac{1}{r}, \quad \beta_3 = 1 \\ \gamma_1 &= 1, \quad \gamma_2 = \frac{1}{r}, \quad \gamma_3 = 1 \\ \zeta_1 &= \frac{1}{r^m}, \quad \zeta_2 = \frac{1}{r}, \quad \zeta_3 = 1 \end{aligned} \tag{42}$$

and $m = 1$ for all equations except the $x_2$ - direction momentum equation, for which $m = 2$. The vector variables used in Eq. 40 are defined as

$$\vec{W} = \begin{bmatrix} \rho U_1 \\ \rho U_2 \\ \rho U_3 \\ \rho \\ \rho h \\ \rho k \\ \rho \varepsilon \end{bmatrix} \qquad \vec{F}_i = r^n \begin{bmatrix} \rho U_1 U_i \\ \rho U_2 U_i \\ \rho U_3 U_i \\ \rho U_i \\ \rho h U_i \\ \rho k U_i \\ \rho \varepsilon U_i \end{bmatrix} \tag{43}$$

where $n = 1$ for $i = 1$ and $n = 0$ for $i = 2, 3$.

$$\vec{P}_i = \begin{bmatrix} p\delta_{i1} \\ p\delta_{i2} \\ p\delta_{i3} \\ 0 \\ 0 \\ 0 \\ \\ 0 \end{bmatrix} \qquad \vec{G}_1 = \begin{bmatrix} r\tau_{11} \\ r^2\tau_{12} \\ r\tau_{13} \\ 0 \\ -rq_1 \\ \frac{\mu_T}{\sigma_k}\gamma_1 k_{,1} \\ \\ \frac{\mu_T}{\sigma_\varepsilon}\gamma_1\varepsilon_{,1} \end{bmatrix} \tag{44}$$

$$\vec{G}_i = \begin{bmatrix} \tau_{i1} \\ \tau_{i2} \\ \tau_{i3} \\ \\ 0 \\ q_i \\ \frac{\mu_T}{\sigma_k}\gamma_i k_{,i} \\ \\ \frac{\mu_T}{\sigma_\varepsilon}\gamma_i\varepsilon_{,i} \end{bmatrix} \qquad \text{for } i = 2,3$$

Note that the velocity components ($U_1$, $U_2$, $U_3$) are the cylindrical-polar velocity components, and $\tau_{ij}$ is the stress tensor written in cylindrical-polar coordinates. The molecular and turbulent stress tensors may be written as

$$\tau_{ij} = 2\mu_{eff}\,\bar{D}_{ij} \tag{45}$$

$$\bar{D}_{11} = \frac{\partial U_1}{\partial \bar{x}_1}$$

$$\bar{D}_{22} = \frac{1}{r}\frac{\partial U_2}{\partial \bar{x}_2} + \frac{U_1}{r}$$

$$\bar{D}_{33} = \frac{\partial U_3}{\partial \bar{x}_3} \tag{46}$$

$$\bar{D}_{12} = \frac{1}{2}\left[r\frac{\partial}{\partial \bar{x}_1}\left(\frac{U_2}{r}\right) + \frac{1}{r}\frac{\partial U_1}{\partial \bar{x}_2}\right]$$

$$\bar{D}_{13} = \frac{1}{2}\left[\frac{\partial U_3}{\partial \bar{x}_1} + \frac{\partial U_1}{\partial \bar{x}_3}\right]$$

$$\bar{D}_{23} = \frac{1}{2}\left[\frac{1}{r}\frac{\partial U_3}{\partial \bar{x}_2} + \frac{\partial U_2}{\partial \bar{x}_3}\right]$$

$$\nabla \cdot \bar{U} = \frac{1}{r}\frac{\partial}{\partial \bar{x}_1}(rU_1) + \frac{1}{r}\frac{\partial U_2}{\partial \bar{x}_2} + \frac{\partial U_3}{\partial \bar{x}_3} \tag{47}$$

The derivatives required in Eqs. 46 - 47 must be expressed in terms of the computational coordinates $y^j$ using the chain rule, (Eq. 32).

Finally, the vector $\vec{S}$ contains source terms and certain differential terms which do not conform to the basic structure of Eq. 40, and the vector $\vec{C}$ contains the additional curvature terms due to the cylindrical-polar coordinate system.

$$\vec{S} = \begin{bmatrix} 0 \\ 0 \\ 0 \\ 0 \\ \frac{Dp}{Dt} + \Phi + \rho\varepsilon \\ \mu_T\,[2\bar{D}_{ij}\,\bar{D}_{ij}\;] \;-\rho\varepsilon - 2\rho\nu\,(\nabla k^{1/2})^2 \\ C_1\frac{\varepsilon}{k}\,[\mu_T(2\bar{D}_{ij}\,\bar{D}_{ij}) + 2\,\mu\mu_T\,(\nabla^2 U)^2 - C_2\,\rho\,\frac{\varepsilon^2}{k}\;] \end{bmatrix} \tag{48}$$

$$\vec{C} = \begin{bmatrix} \frac{1}{r}\rho U_2^2 - \frac{1}{r}\bar{\tau}_{22} \\ -\frac{1}{r}\rho U_1 U_2 \\ 0 \\ 0 \\ 0 \\ 0 \\ 0 \end{bmatrix}$$

Since the cases described in this report have widely differing geometry, specific details of the grid transformations will be postponed until each case and its results are described in detail in subsequent sections.

Solution Procedure

The solution procedure used to solve the governing equations detailed previously is the linearized block implicit (LBI) method of Briley and McDonald [15, 16], which has been applied to numerous other problems. A detailed explanation of this method can be found in the work of Briley and McDonald [15, 16]. Repetition of this is unwarranted here; instead a summary of the method can be found in the appendix to this report. This appendix also contains sections dealing with linearization and time differencing, treatment of diffusive terms and the splitting scheme of the LBI method.

## DISCUSSION OF RESULTS

Under the present effort a variety of test cases have been performed in order to investigate various aspects of both steady and unsteady shock wave-boundary layer interactions. These cases, which are summarized below, are discussed in detail in this section. For clarity, geometry descriptions and boundary condition specification are described subsequently for each case. The cases presented are axisymmetric unless otherwise stated, and are as follows:

(i) A normal shock wave-boundary layer interaction in a tube ($M_\infty \simeq 1.44$);

(ii) Steady transonic flow over a bump ($M_\infty \simeq 0.875$);

(iii) Unsteady transonic flow over a bump ($M_\infty \simeq 0.875$, reduced frequency $\simeq 0.175$ and $0.004$);

(iv) Flow over a compression ramp ($M_\infty \simeq 2.0$);

(v) Shock impingement on a flat plate boundary layer flow ($M_\infty \simeq 2.0$).

### Normal Shock Wave-Boundary Layer Interaction in a Constant Area Tube

Normal shock-wave-boundary layer interaction is a frequently occurring phenomenon in aeronautical applications. The flow field contains a complex set of phenomena including shock waves, boundary layers in adverse pressure gradients and possibly a zone of separated flow. Even in cases where the shock pattern is essentially steady, the sudden wall static pressure rise accompanying the interaction can lead to significant unbalanced forces, and the high heat transfer rates typically present in non-isothermal flows at flow reattachment can lead to structural problems. The first case considered simulates a normal shock wave-boundary layer interaction occurring at modest supersonic Mach number in a tube of constant circular cross section. The case has been specified to coincide with the experimental data of Mateer, Brosh and Viegas [30]. These experimental results are available in sufficient detail to enable detailed comparison between experiment and prediction to be performed.

The calculation was performed for an inlet Mach number of 1.44 with an imposed exit to inlet pressure ratio of 2.0 and a Reynolds' number based on upstream boundary layer thickness of $5.83 \times 10^5$. The inlet boundary layer thickness which was 2.5 cm was also used as the reference length for the calculation.

Boundary Conditions

A major factor in obtaining efficient solutions for the Navier-Stokes equations is specification of appropriate boundary conditions. Boundary condition specification, which has been the subject of considerable effort in recent years, essentially imposes the effect of the environment in regions outside the computational domain on the problem being investigated. Specification of boundary conditions at walls is relatively straight forward, but proper specification at inflow and outflow boundaries presents a more difficult problem. The present effort follows the work of Briley and McDonald [33] who suggest examining the characteristics of the inviscid problem for guidance at inflow and outflow boundaries. Since at a supersonic inflow boundary all dependent variables can be specified and since at a subsonic outflow boundary only one dependent variable can be specified, boundary conditions were set as follows:

(i) Upstream (supersonic inflow) boundary -
Function boundary conditions for each dependent variable ($u$, $w$, $\rho$, $h$, $k$ and $\varepsilon$) with profiles consistent with experimentally determined values [30].

(ii) Downstream (subsonic outflow) boundary -
Second derivative of $u$, $w$, $h$, $k$ and $\varepsilon$ set to zero.
Static pressure specified.

(iii) Wall boundary -
No-slip (i.e. function values $u = w = k = \varepsilon = 0$).
Normal Momentum equation.
Adiabatic Wall.

(iv) Symmetry Plane -
Function value $u = 0$.
First Derivative of $w$, $\rho$, $h$, $k$ and $\varepsilon$ set to zero.

A second major consideration in obtaining accurate numerical simulations of flow situations is specification of a proper computational grid. Obviously, code size, computer core size, computer run costs, etc. dictate that the number of computational grid points used in performing a calculation be minimized. However, in most flow situations not all regions

of the flow require the same grid resolution. In regions containing boundary layers or shock waves dependent variables change rapidly with physical distance and these flow regions require high grid resolution. Other flow regions may be satisfactorily resolved with a considerably sparser grid point density. As previously described, the governing Navier-Stokes equations are written in a general coordinate system. However, before performing a specific calculation a coordinate system transformation suitable for the problem at hand must be provided. Many possible methods are available for grid generation, but in this example where both boundary geometry and flow structure conform to well defined, geometric shapes, construction of the coordinate system is preferable.

For the axisymmetric normal shock problem of this section, a stretched Cartesian grid has been used in the symmetry plane. For this purpose, a modification of the method of Roberts' [31], was employed. This approach uses a sinh function for the purpose of clustering points in the interior of a domain, to resolve the shock gradients, and a tanh function at boundaries to resolve boundary layer gradients. A typical example of the grid, at a particular time, is given in Figure 1. It should be noted in this connection that care must be exercised in using the sinh function, since excessive stretching can lead to the introduction of large spatial truncation errors.

Solution Adaptive Coordinate System

Specification of high grid resolution in the vicinity of a no-slip wall is obviously required to resolve a boundary layer. However, specification of a high resolution region to resolve a shock is not as simple a problem. In some flow situations, both the shock location and angle can be well estimated and in these cases an accurate, a priori judgment can be made in specifying the region of high resolution. However, in many cases the situation is not clear because the shock location and/or its shape may not be known a priori. Since adequate grid resolution in the shock region is required to obtain sharp solutions without spurious spatial oscillations, an alternative procedure must be used. In the present case, a normal shock was expected in the tube. Therefore, an orthogonal system with one set of coordinates parallel to the wall and one set normal to the wall would be appropriate if proper regions of high resolution could be obtained to resolve the shock.

With the basic form of the coordinate system established, a viable shock tracking strategy was developed using the wall pressure gradient and pressure rises to determine the shock location. In particular, a search for the maximum pressure gradient location was used to establish a definition for the shock center. In the early stages of calculation a "noisy" solution often exists. Any spurious oscillations in the solution would prove detrimental to accurate shock center determination since large gradients are possible and could conceivably exceed the gradient at the actual shock center. In order to avoid this possibility, a "filtering scheme" was applied to the process of shock location. Figure 2 demonstrates diagrammtically the relevant features of the search and filtering processes. In addition to the filtering applied to the adaptive grid shock location scheme, the movement of the mesh was controlled. This was achieved by allowing only limited mesh movement at each time step. This avoids the introduction of excessive temporal truncation error which could slow convergence.

Essentially, the procedure identifies turning points in the wall static pressure distribution, examines the change in pressure between subsequent turning points and carries out a search for the maximum pressure gradient in the interval having largest pressure rise. Sections having negative pressure gradient are ignored for this particular problem. This approach assumes that the shock is centered at the point of maximum streamwise pressure gradient in the interval having the largest positive pressure increase. This effectively filters out all but the most significant pressure rise which is assumed to be the rise due to the shock. In more general cases where multiple shocks occur or where separation and reattachment give rise to a plateau in the pressure distribution a less restrictive filter would be required if resolution of each significant pressure rise is desired. A significant pressure rise is of course problem dependent, therefore, general guidelines are difficult to prescribe.

Once the shock center was located, a new grid was constructed by centering the sinh function at the new shock location. The transverse grid was not changed in the normal shock calculation even though local boundary layer thickening occurs in the interaction zone. However, the transverse grid transformation was constructed to take account of the expected thickening and thereby ensure adequate boundary layer resolution throughout the calculation domain. The entire process of establishing the shock

location and constructing a new grid was performed explicitly, after each time step, and as a consequence the grid motion lags the shock motion. The grid motion was accounted for in the governing equations through inclusion of terms containing derivatives of computational coordinates with time.

## Results

The present case was run with two different turbulence models. These were a mixing length model, and a $k - \varepsilon$ model; both of which have been described earlier. Before beginning the calculation, an initial, consistent approximation to the flow field was constructed. This was obtained by assuming the Rankine-Hugoniot relations for both static pressure and velocity ratios across the shock, at an assumed streamwise location, and applying a tanh function to blend the upstream and downstream values for a given transverse location. By also assuming constant total enthalpy and a specified upstream velocity profile, a consistent initial flow field was obtained. The assumed shock location did not take into account the influence of the boundary layer on shock location and as expected, the shock location began to move upon initiation of the calculation. In order to maintain adequate resolution in all phases of the calculation, the adaptive mesh strategy described earlier was invoked. The calculation was first performed on a computational grid with 41 transverse and 31 streamwise points, using the mixing length turbulence model described earlier. This calculation converged within 150 time steps with an overall reduction in the maximum residual in the field of two orders of magnitude. The residual was monotonically decreasing with increase in time and the solution was stationary when the calculation was terminated.

The results obtained are shown in Figs. 3 and 4 along with those obtained using a two-equation, $k - \varepsilon$ turbulence model. In the current work an intermediate calculation was also performed using a one-equation, $k - \ell$ model. This additional calculation was performed in order to obtain a suitable initial k field for use in starting the $k - \varepsilon$ model prediction. However, more recent work indicates that the additional step is not necessary and that the $k - \varepsilon$ calculation can be performed by using the mean flow obtained using mixing length assumptions and using initial approximations for k and $\varepsilon$ determined from algebraic relations. Results obtained using both mixing length and $k - \varepsilon$ models are shown in Figs. 3 - 4 which also show comparison with experimental data, for the wall static pressure through the

interaction zone and velocity profiles at the streamwise locations indicated in Fig. 4. Figure 5 shows the shear stress profiles evaluated from the $k - \varepsilon$ results. Closer examination in Fig. 3, which shows the wall static pressure distribution in the interaction zone, reveals good agreement with experimental data using both turbulence models. Figure 4 shows velocity profile plots at four streamwise locations. Once again, agreement between prediction and experiment is good with the mixing length model producing slightly better results.

In performing this calculation the artificial dissipation parameter $\sigma$, designed to remove pre- and post-shock induced spurious oscillations and described in the appendix, initially had a value of 0.5. Such a relatively large value certainly smears out spurious solution oscillations, but can also modify the solution unrealistically. Therefore, after convergence with $\sigma = 0.5$ its value was reduced to 0.05, which is a relatively small value, in order to ensure an accurate solution free from arbitrary smearing. Values in the range $0.025 \leq \sigma \leq 0.1$ have been used by the authors with good results for a variety of flow problems [42], and generally a further reduction below $\sigma =$ .05leaves the solution unaltered with eventually the spurious oscillations returning as $\sigma \to 0$.

It can be seen that mean flow quantities are well predicted by the method, but apparent discrepancies exist in the prediction of Reynolds shear stress profiles, Fig. 5. This is particularly true at $z/\delta = 4$ which is very close to the interaction zone. It is interesting to note that the predictions of Mateer, et al [30] show a similar disparity. It should also be noted that the turbulence measurements were obtained using hot wire anemometry, and as indicated by Mateer, et al [30] it is difficult to determine the sensitivity of hot wire probes to velocity and density changes in transonic flow. The discrepancy occurs in the region of the shock boundary layer interaction where density and velocity gradients are most significant. As a consequence, the experimental turbulence data must be viewed with caution in this area. In addition, the apparent rapid dissipation occurring within $4\delta_\infty$ of the interaction region seems unrealistic and inconsistent with known turbulence processes (Fig. 5). The problem of ascertaining the cause of the discrepancy would be difficult to resolve without the use of non-intrusive turbulence measuring techniques.

To gain additional insight into the normal shock wave-boundary layer interaction process, it is informative to examine contour plots of static pressure and Mach number. Figure 6 shows static pressure contour plots of the whole solution domain in conjunction with a coordinate system plot showing the relative locations of grid clustering and shock location. It can be seen that a sharp (shock) pressure rise, extending across only eight streamwise grid points is predicted in the free stream region, and that the effect of its interaction with the boundary layer is to diffuse the shock and form a characteristic lamda foot near the wall. Figure 7 shows the static pressure in the interaction region in more detail. Figure 8, which presents velocity vectors in the shock region indicates the displacement of the boundary layer which results from the interaction process. It should be noted that the present calculation strategy ignores the possible shock discontinuity and instead continues to assume the solution can be expanded in a Taylor series in this region. The present procedure 'shock captures' rather than 'shock fits'. In the particular flow studied, the moderate super-sonic Mach number encountered, the presence of the boundary layer, and the confined nature of the flow all help ensure that in reality a sharp discontinuity in the flow is not encountered, thus justifying the 'shock capturing' approach.

The normal shock boundary layer interaction prediction described above demonstrates, by comparison against experimental data, an ability to accurately and economically predict transonic shock wave-boundary layer interaction. The problem, though conceptually simple, provided a means of validating the correct operation of the code and the various changes incorporated to allow for the treatment of shock waves. The great similarity between the results obtained using the simple mixing length and the $k - \varepsilon$ models is not surprising. This is because the mixing length was originally developed for attached boundary layer flows and, at least in regions outside the interaction zone, the problem considered contains discernable boundary layer characteristics. Nevertheless, the problem provided a useful test of the $k - \varepsilon$ model for which the mean flow results show equally good agreement with data. It may be concluded from the results of this case that for related normal shock wave-boundary layer interaction problems in which no flow separation occurs use of a mixing length model will provide acceptable results.

## Steady Transonic Flow Over an Axisymmetric Bump

The second portion of the present effort focused upon the effect of longitudinal curvature on the shock wave-boundary layer interaction process. This was done by considering the problem of steady transonic flow over an axisymmetric bump. The first case in this portion of the study was based on the experiment of Johnson and Horstman [32]. In this same reference, Johnson and Horstman also report the details of their own calculation for the same problem. The current calculated results for the Johnson-Horstman case are compared with both experiment and the calculation reported in Ref. 32. The remaining steady transonic bump calculations reported are variations of this original case, and demonstrate the effect of increased approach boundary layer thickness and of longitudinal wall curvature on shock inducement and the shock wave-boundary layer interaction process.

Each case of the series of three cases was performed with an approach Mach number of 0.875 with the bump mounted on a cylinder. The experimental arrangement, shown in Fig. 8, used a hollow, thin-walled cylinder to avoid cylinder leading edge effects influencing the interaction process. Therefore, in simulating this experiment, a negligibly thin approach boundary layer was specified at the upstream boundary. The bump considered is a circular arc with its leading edge joined smoothly to the cylinder surface by a circular arc fillit. Using the chord length of the bump as the reference length, the relative dimensions of the problem are indicated in Fig. 9. The upstream distance from the bump leading edge to the inflow boundary was chosen to allow development of a boundary layer velocity profile consistent with that of the experiment. The other steady cases completed, although not compared to experiment, are compared to the first case in order to demonstrate in general terms the effects of increased inlet boundary layer thickness and of increasing the wall curvature. The boundary conditions for all three cases were the same and are described in the following section.

### Boundary Conditions

Following Briley and McDonald [33] analysis of the characteristics for the bump problem shows that for the cases of interest where the inflow and outflow are subsonic and the supersonic patch expected in the vicinity of the bump does not extend to the top boundary of the solution domain the following boundary conditions are appropriate.

(i) Upstream (subsonic inflow) boundary -

Function condition on u-velocity (transverse velocity).

Two layer model on w-velocity and static enthalpy [33]. See following text for a brief explanation.

Second derivative of static pressure set to zero.

(ii) Downstream (subsonic outflow) boundary -

Second derivative of u, w and h set to zero.

Static pressure specified.

(iii) Wall boundary -

No-slip on u and w.

Normal momentum equation.

Wall temperature specified.

(iv) Freestream Boundary -

u set to zero.

First derivative of w, $\rho$ and h set to zero, simulating a free slip-wall condition.

The so-called two-layer model [33] used at the inflow boundary is essentially a total pressure boundary condition applied to the core flow with a specified boundary layer profile shape for the wall region. Matching the static pressure at the edge, defined by the first computational point from the wall at which $|w|/|w|_{max}$ was greater than or equal to 0.99 on the previous time step, enables calculation of $|w|$ at this point. This provides the required normalizing value for the pre-specified boundary layer profile shape. Overall, the method provides a mechanism for drawing mass flow in order to satisfy the downstream pressure given an upstream core total pressure. This specification corresponds to the usual wind tunnel experiment where stagnation conditions are set in an upstream reservoir and static pressure is set at some downstream location. Specification of an inlet mass flux could be accomplished indirectly by varying the downstream static pressure, otherwise attempts to specify an inflow mass flux directly leads to numerical problems.

(i) Large Radius of Curvature Bump; Thin Inlet Boundary Layer

This case, for which experimental data are available, simulates flow of a developing boundary layer over a moderately thin axisymmetric bump. Before beginning the calculation, an appropriate initial flow field was constructed. This was achieved by imposing a linearly varying static pressure

drop between inlet and exit in addition to an assumed upstream velocity profile. The boundary layer thickness upstream was set to a value of 0.0009c where c is the bump chord length and this was found to give a boundary layer growth matching that of the experiment at 0.25 chords ahead of the bump leading edge. This was determined by comparing the computed and experimentally reported velocity profiles at this location. The details of the flow field were then obtained by assuming flat plate flow and constant total enthalpy with density obtained via the equation of state. A constructive technique was used to generate a computational grid of 31 transverse and 51 streamwise points. Later the number of grid points in the streamwise direction was reduced to 46 for reasons discussed subsequently.

The distribution of streamwise grid points for this problem was a compromise between the desire to resolve the region of flow acceleration over the bump and the region of deceleration through the shock and the need to maintain an economical calculation. In view of this, the final coordinate system used has one region of streamwise grid refinement. This region spans the bump chord and has a minimum grid spacing of 0.037c at the trailing edge, compared with a local maximum grid spacing ahead of the bump of 0.523c, and of 0.166c aft of the bump. The starting flow field for this case was constructed by assuming the flow field to be zero pressure gradient flat plate boundary layer flow. In other words a self similar velocity profile was distributed throughout the domain with density, enthalpy and pressure specified consistently. No attempt was made to introduce an initial shock but rather the flow structure was allowed to develop with time. Having established a suitable starting flow field, the calculation was begun. Solution convergence was achieved within about 150 time steps at which point the maximum residuals of the problem had been reduced by two orders of magnitude. It should be noted that the calculation at this time was changing about some mean state with a maximum amplitude of about 1%. No detailed study of accelerating convergence was made and it is possible that convergence could be obtained with significantly fewer time steps. In the final calculation the artificial dissipation parameter, described in the appendix, was set at 0.05. The calculation was performed using a mixing length model to account for turbulent viscosity variations and was subject to the boundary conditions outlined in the previous section. The upstream Mach number was 0.875, but acceleration over the curved surface of the bump lead to locally supersonic flow.

The streamwise wall static pressure distribution predicted by the current method is presented and compared, in Fig. 10, with both the experiment and calculations of Johnson, Horstman and Bachalo [32]. It is immediately apparent that agreement with experiment is not good in the interaction region. The predicted pressure distribution indicates a shock location significantly further downstream than that seen experimentally. Similar disparity is evident in the results of Johnson, et al who attribute the discrepancy to inadequacy of the turbulence models used in their calculations. Johnson, et al [32] used two different models: the first being the Cebeci-Smith [34] mixing length model and the second the two-equation model of Wilcox-Rubesin [35]. In view of the close agreement between these two calculations obtained by Johnson, et al [32], it seems unlikely that turbulence modeling is the key to resolving the major discrepancy between calculation and experiment. In support of the last statement, and purely for demonstration purposes, a laminar flow calculation was performed using the method of this report and subjected to the same inlet conditions, boundary conditions and pressure ratio of the turbulent case. For laminar flow at the same Mach number as the turbulent case it is expected that the shock would adopt a position closer to the leading edge of the bump. Therefore, a laminar calculation should indicate the possible sensitivity of the calculation to the turbulence model. Although the laminar calculation indeed moved the shock forward and consequently moved the results closer to experiment, the movement was not sufficient to come close to matching the data. Since the laminar case represents an extreme perturbation in the viscosity, and since the two calculations of Ref. [32] and the turbulent calculation presented here are essentially in agreement, it seems unlikely that physically reasonable perturbations of a turbulence model would produce better agreement.

More likely as an explanation is that insufficient experimental downstream flow and geometry details were provided, leading to the application of incorrect downstream boundary conditions and geometry modeling in both the Johnson-Horstman calculation and that reported here. It should also be noted that Johnson and Horstman [32] applied downstream boundary conditions at a distance of 4.4 chords from the leading edge in order to be able to apply first derivative boundary conditions. In order to justifiably assume that flow variables were not changing at the downstream boundary, they recalculated the flow with the boundary at different locations and imposed

the same boundary conditions. However, even though they observed substantially unchanged results, it should be noted that the downstream boundary of their calculation was placed about 2 chords further downstream than the diffusing section present in the experiment and as a result did not take into account the change in pressure expected in the transition to the diffuser, shown in Fig. 9.

In the case of the current calculation, the downstream boundary conditions were initially applied at about 4 chords downstream of the leading edge of the bump and the magnitude of the static pressure was obtained by extrapolation from the experimentally determined value at 1.5 chords assuming, as Johnson et al implied, that the pressure profile was flat beyond that location. This was necessary due to the lack of experimental data at the end of the cylindrical section, approximately 2.5 chords aft of the leading edge. In order to demonstrate the importance of appropriate downstream boundary conditions, two additional calculations were performed in which the downstream boundary was located at 2.67 chords aft of the leading edge. In this case, the number of streamwise grid points was cut to 46. These were performed with the same boundary conditions as described previously but with the imposition of upstream to downstream static pressure ratios of 1.0 and 1.05, respectively.

The wall static pressure for both of these cases is shown superimposed on Fig. 10. It can be seen that with the downstream boundary located at the start of the diffusing section of the experiment, and an exit static pressure of 1.05, the wall pressure profile is modified and the start of the pressure rise is significantly further forward than in the case with the downstream boundary at 4 chords aft of the leading edge. With a pressure ratio of 1.05 better agreement with the experimental data is achieved. Even though the minimum and maximum pressures are greater than given by the data, the relative shock location is correct. These calculations clearly demonstrate the sensitivity of this transonic flow configuration to the downstream conditions.

Figures 11 and 12 show constant static pressure and Mach number contours respectively and are presented in order to demonstrate the flow behavior. Examination of the static pressure contours in Fig. 11, shows the expected expansion as the flow accelerates over the bump, followed

by a shock as the flow turns back parallel to the cylinder wall. For this case flow separation is of limited extent with the separation point being at z/c=0.69 while reattachment occurs at z/c=0.9. Velocity vectors are shown in Fig. 13.

An additional important point to note in this series of cases is the position of the separation and reattachment points since the effective wall shape downstream of the acceleration determines the shock location which in turn affects flow separation due to the adverse pressure gradients associated with it.

(ii) Large Radius of Curvature Bump; Thick Inlet Boundary Layer

This second axisymmetric bump case was performed in order to demonstrate, in general terms, the effect of increased approach boundary layer thickness on the transonic shock wave boundary layer interaction. The bump geometry used was identical to that described previously and the calculation was performed with the imposition of an inlet to exit static pressure ratio of 1.0. In addition, the boundary layer thickness imposed at the upstream boundary was increased from 0.0009c to 0.049c. Figures 14 and 15 show the constant static pressure and Mach number contours for the thick boundary layer case. Comparing Figs. 11 and 14 it can be seen that the shock in Fig. 14 is located further forward than that in Fig. 11, and that it extends further into the free stream. The thick boundary layer shock is weaker and the shock shape closer to vertical, thus indicating boundary layer thickness has an effect on strength and shape. In addition, examination of the Mach number contours reveals an extensive separation in Fig. 15 which significantly modifies the displacement surface. The increased boundary layer thickness associated with this is evident in Fig. 16, which shows velocity vectors at selected stations. Comparisons of wall static pressure distributions will be discussed subsequently.

(iii) Small Radius of Curvature Bump; Thin Inlet Boundary Layer

In order to demonstrate the effect of bump longitudinal curvature on shock wave-boundary layer interaction, one final steady flow case was performed in which the thin inlet boundary layer of the original case was imposed at the upstream boundary and an inlet to exit static pressure ratio of 1.0 was imposed. These conditions were imposed on a cylinder/bump

configuration for a bump having a radius of curvature of 0.59c compared with 1.35c for the large curvature cases above. Figures 17 and 18 present constant static pressure and Mach number contours respectively while Fig. 19 shows velocity vectors at selected streamwise locations. It can be seen, as expected for the larger bump, that a pronounced separation occurs at the bump trailing edge. In addition, while a shock exists it does not extend very far into the core flow. However, by comparison with the original case, having large radius of curvature and thin approach boundary layer, the start of the pressure rise is located significantly closer to the bump leading edge at about $z = 0.7c$. Again the details of the shock pattern including strength and shape appear sensitive to geometry.

Steady Transonic Flow Over an Axisymmetric Bump: Summary

Among the main observations to be derived from the foregoing discussion of results are the following. In performing calculations of this type it is very important to accurately model the downstream boundary conditions. This has been demonstrated in the calculations of the Johnson-Horstman bump problem. As has been shown in Fig. 10, specification of downstream boundary conditions appears to have a much more significant impact upon results than reasonable (or even drastic) changes in turbulence model. Also, it appears that the position of the induced shock is largely determined by the location and extent of the flow separation, which in turn depends upon the shock strength. Thus, an analysis containing these mutually dependent effects is required to obtain meaningful predictions. In general, both increased approach boundary layer thickness and more severe wall curvature tend to move the separation point forward since even without the shock both give rise to earlier separation. Increased approach boundary layer thickness gives rise to premature separation because of the boundary layers inability to sustain the adverse pressure gradient associated with the flow deceleration through the shock. Increased curvature gives rise to more severe acceleration and deceleration and consequently more severe adverse pressure gradients which also adversely affects the ability of the boundary layer to avoid separation. The presence of the shock which appears as a result of turning the locally supersonic flow enhances the pressure gradients giving rise to some modification of the location of the separation, and its extent.

Figure 20 gives a comparison of the wall pressure distribution for each of the above cases. It is apparent that the case having a smaller radius of curvature bump yields a pressure distribution consistent with intensive flow acceleration over the bump. This is indicated by the significantly lower-minimum wall pressure achieved. Both this case and the case having a thick approach boundary layer exhibit flattening of the pressure rise typical of that occuring when shock induced separation occurs. The start and end of this "plateau" coincides in these calculations with the separation and reattachment points. No such flattening is apparent in the larger radius of curvature, thin boundary layer case which is consistent with the lack of significant separation in this case. Considering the overall wall pressure distribution, it appears that the wall pressure is more sensitive to changes in the bump curvature than to changes in the boundary layer thickness. This indicates bump curvature may be an extremely important parameter in axisymmetric interactions.

## Unsteady Transonic Flow Over an Axisymmetric Bump

Unsteady transonic flow is a frequent occurence in aeronautical engineering applications, and consequently prediction of such phenomena are of interest. Examples of unsteady transonic flow are the helicopter rotor field, the surge phenomenon occurring in transonic turbomachinery flows and flight control surface buzz. Therefore, under the present effort, cases of unsteady transonic flow were considered with the major aims being to demonstrate unsteady transonic flow calculations and consider both a quasi-steady and time-dependent flow configuration using the time-dependent Navier Stokes equations. The specific flow configuration considered was obtained by imposing a periodically perturbed exit static pressure on transonic flow over an axisymmetric bump. The bump geometry modeled is identical to that described earlier in which a large radius of curvature bump was mounted on an axisymmetric cylinder, with negligibly thin approach boundary layer.

The boundary conditions for this problem were described earlier with the exception of the exit static pressure boundary condition. The exit static pressure was applied as a time-dependent function of the form:

$$p(t) = p + \Delta p \cdot \cos(\omega t)$$

where $\bar{p}$ is the mean exit pressure, $\Delta p$ is the perturbation amplitude, $\omega$ is the frequency and t is time. Rather than use $\omega$, it is convenient to introduce the reduced frequency $f_r$ based upon boundary layer scales defined as $\omega\delta_\infty/U_\infty$ where $\delta_\infty$ is the boundary layer thickness at the leading edge of the bump and $U_\infty$ the edge velocity at this same location.

For the two cases described here, $\bar{p}$, = 1.05, $\Delta p$ = 0.05 and $f_r$ = 0.175 and 0.004.

(i) High Frequency Case ($f_r$ = 0.175)

The unsteady flow cases described here were performed using a mixing length model to account for variations in turbulent viscosity. Use of such a simple model seems reasonable in this case since the main aim is the economical demonstration of the capability of the present method to compute periodically unsteady flows and to examine the effect of frequency upon the flow. Furthermore, appropriate time-dependent multi-equation models are not yet well established. The starting flow field for this case was the converged steady case described previously in which the pressure ratio was set to 1.0, but as noted in the introduction to this section, the time mean pressure for these cases was set to 1.05. However, starting the calculation such that the initial exit pressure for the case was 1.0 assured a gradual transition from steady flow to unsteady flow calculation. In other words the calculation was begun at a turning point in the exit pressure temporal variation; i.e., $dp_e/dt=0$. Examination of the time history of the wall static pressure, given in Fig. 21, reveals the frequency response of the flow to cyclic variation in the imposed pressure ratio. Shown in the figure are the static pressure variations at the three locations indicated. These locations are at the downstream boundary, at z/c = 0.75, the steady flow shock location and at z/c = 0.61 the experimentally determined steady flow shock location. The latter two locations were chosen for convenience and are not, of themselves, of major physical significance. The initial wall pressure transient is a response to the newly imposed mean pressure ratio and takes $7\pi$ radians before the first turning point is reached. Between $7\pi$ radians and $10\pi$ radians the response of the wall pressure at z/c = .75 developed a periodic

oscillation corresponding to the sinusoidal oscillation of the back pressure. Examination of the response at the start of the pressure rise at z/c = .61 shows no appreciable variation once the initial transient adjusting the mean pressure is over. The implication is that after adjusting to the new mean value, the shock location is essentially unaffected by downstream oscillations at this frequency. That is at this relatively high frequency of oscillation disturbances propagated upstream from the perturbed exit pressure are attenuated by the shock and as such do not affect the shock location. Comparison of this result, at the instant at which the pressure ratio is about 1.05, with the steady state solution having a pressure ratio of 1.05 shows no appreciable difference in the wall static pressure profile in the vicinity of the shock.

(ii) Low Frequency Case ($f_r$ = 0.004)

In order to show the flow phenomena for a much reduced exit forcing frequency a low frequency case was initiated. This calculation was begun by restarting from the previous high frequency case but with the new frequency imposed on the exit pressure variation. For this case, as in the previous case, the mean static pressure at exit was 1.05 and the amplitude of the oscillation was 0.05. However the reduced frequency of oscillation was reduced to 0.004 in order to attempt to appreciably influence the location of the shock. Modifying the frequency of oscillation instantaneously introduces a transient into the calculation, which was allowed to develop over several cycles before a periodic response to the oscillating exit pressure was detected. Two additional cycles were then computed in order to verify periodicity. Figure 22 shows the wall static pressure variation at a number of streamwise locations including the exit plane. This figure indicates periodic response to the exit forcing frequency, but Fourier analysis of the results also reveals that the response in the vicinity of the shock contains higher harmonics which tend to distort the response locally. In support of this, Figure 23 shows the streamwise variation in amplitude of the primary and first harmonics of the wall static pressure response. It can be seen that far upstream and downstream the response remains almost purely sinusoidal since the first, and higher harmonics are negligible. However in the vicinity of the shock the amplitude of both the primary and first harmonics peak dramatically. This is an expected result of the motion of the

shock since in the vicinity of the start of the shock the time mean pressure profile exhibits a minimum; and with the shock oscillating about its time mean location, wall points in this vicinity ($z/c \approx 0.61$) experience a wider range of pressure variation than those upstream and downstream of the bump where the time mean pressure profile is a relatively slowly varying function of $z/c$. It is also interesting to note that the time mean pressure profile is indistinguishable from the steady flow pressure profile having an exit pressure of 1.05. Figure 24 shows a sequence of static pressure contour plots for this problem and indicates the movement of the shock as a function of time.

## Unsteady Flow Cases: Summary

The unsteady, transonic flow calculations performed and reported in the previous section are for two reduced frequencies in the high and low range respectively. It is observed that for high frequency of exit pressure oscillation modification to the flow field are confined to the vicinity of the downstream boundary. The shock location is unaffected by the perturbations. In contrast the low frequency case, having the same forcing function amplitude, exhibits a periodic response to the downstream pressure fluctuations. This case in which the shock moves periodically about its time mean location produces large (by comparison with the input) amplitude fluctuations in the vicinity of the shock's time mean location.

## Steady Flow Over An Axisymmetric Compression Ramp

Many workers have addressed the problem of calculating oblique shock wave inducement at two-dimensional compression corners in supersonic approach flow [9]. However, the axisymmetric compression corner problem has received little attention. Therefore, as part of the present effort consideration was given to the problem of axisymmetric compression corners. Before performing the calculation, which in this case was for an approach flow having a Mach number of 2.0 and a 23° axisymmetric compression ramp, a suitable starting flow field and coodinate system were required. In constructing the coordinate system use was made of the known exact incompressible potential flow solution for flow over an axisymmetric ramp in order to generate the streamwise coordinate lines. Adopting the streamlines obtained from the potential flow solution and applying an appropriate grid stretch in the transverse direction to resolve the boundary layer region provided one family

of coordinate lines. The transverse coordinate lines were obtained by defining the end points of an assumed oblique shock at an angleextracted from the inviscid shock wave relations, and using these points on the top and bottom boundaries as the centering location about which the remaining streamwise grid points are clustered. The second family of coordinate lines, therefore consisted of a series of straight lines joining points on the top and bottom boundaries of the computational domain, Fig. 25. These lines are vertical at the upstream boundary but as a result of applying different grid stretching on the top and bottom boundaries the angle each line makes with the horizontal varies throughout the computational domain such that, in the vicinity of the expected shock, the grid lines align with the shock direction. At the downstream boundary coordinate lines are once again vertical. Having generated the grid the initial velocity field was aligned in the direction of these coordinate lines. To account for the expected shock the initial flow field was constructed by considering the flow field to consist of three zones. In the first, upstream, zone pre-shock velocities and pressures where applied. Downstream post shock values where obtained from the shock relations, and in the intermediate region upstream and downstream values were smoothly blended to avoid an initial discontinuous representation of the shock. Having determined both the velocity and static pressure fields, the assumption of constant total enthalpy was invoked to enable the density and temperature fields to be determined.

The resulting flow field constituted a reasonable approximation for use as the initial flow field for the problem. The calculation initiated from this flow field converged within 150 time steps; although in developing the strategy for running the case approximately 500 time steps were performed, it is estimated that to rerun the same or a similar calculation with all the appropriate changes incorporated 150 time steps is a realistic estimate for convergence. At convergence, the maximum residuals for the problem had been reduced by two orders of magnitude, at which point the maximum change in the solution on subsequent time steps was less than 1 per cent, and was continually diminishing with time.

The boundary conditions used for the wedge problem were based upon a characteristic analysis of the inviscid flow equations which indicates that

for the equations used four physical conditions are appropriate at the upstream boundary. The conditions specified for the problem were:

(i) Upstream (supersonic inflow) boundary -
Function conditions on u-velocity and w-velocity with a bounday layer profile specified.
Function conditions on density and enthalpy.

(ii) Downstream (supersonic outflow) boundary -
All dependent variables extrapolated by imposing zero second derivatives.

(iii) Wall boundary -
No-slip on u- and w-velocities.
Normal derivatives of static pressure and enthalpy set to zero.

(iv) Free stream boundary -
First derivative in the coordinate direction set to zero for all dependent variables.

The assumption made in applying the above free stream boundary conditon is that ahead and after the shock, the free stream is expected to be inviscid and approximate slug flow. In addition, in the vicinity of the shock flow variables in the direction along the shock do not vary. Therefore, by arranging the coordinate system to align with the shock enables extrapolation from the field to the free stream boundary in the coordinate direction to be a reasonable boundary condition.

The results presented are for a calculation in which the mixing length model described earlier has been used to represent the effect of turbulence on the mean flow development of supersonic flow over an axisymmetric compression ramp. These results are shown in Figs. 26 to 28 and include wall and freestream static pressure distribution, constant density and constant static pressure contours. Examination of Figs. 26 and 27 show a sharp shock located at the corner. The upstream influence of this corner is, as expected, very limited with a marginal increase in pressure ahead of the corner.

The wall static pressure distribution of Fig. 28 shows a very sharp pressure rise to a peak pressure of 2.65. The rise in pressure does not exhibit the plateau often expected in induced shock flows. In general, such a plateau is indicative of a separation region. In this case, a very small separation zone exists with separation and reattachment at $z = -0.23$ and

0.023, respectively. At reattachment, the pressure begins to fall smoothly and monotonically down to a level of 2.35. In contrast to the sharp shock indicated by the wall static pressure distribution the pressure distribution at the freestream boundary shows a steady rise in pressure through a relatively diffuse shock with a maximum pressure of 2.2. This pressure rise corresponds to an expected inviscid pressure rise of 2.24. These results were obtained with the artificial dissipation parameter $\sigma$ set to 0.1 which experience has shown to be a low value. Significantly, the results are free of spurious oscillation in spite of this low artificial dissipation. Experience with other similar codes has shown $\sigma = 0.1$ to produce acceptable solutions which compare well with data.

In the case described here the lack of experimental data prevents comparisons but in general it can be stated that the solutions appear physically plausible.

## Oblique Shock-Wave Impingement on a Flat Plate Boundary Layer

While the supersonic flat plate boundary layer shock impingement problem has been addressed by a number of workers employing Navier-Stokes analyses, e.g. [36], most have used a Cartesian coordinate system on which to perform their calculation. The main criticism of these calculations centers around the shock capturing used to treat the impinging and reflected shocks. The use of a Cartesian grid to predict an oblique shock can result in spatial truncation error problems as a result of poorly resolving the shock. In order to alleviate such problems, a coordinate system was devised which aligns with both the impinging and reflected shocks thereby maintaining adequate resolution of both shocks with a limited number of grid points, Fig. 30.

A calculation was performed with this coordinate system for a freestream Mach number $M = 2.96$ and an impinging shock wave created by a $10.89^\circ$ shock generator. The Reynolds number was sufficiently high so that the flow was turbulent, and a mixing length turbulence model was employed. The coordinate system shown in Fig. 30 was allowed to adapt to the impinging and reflected shocks so that very sharp shock definition was obtained, as shown by the pressure contours in Fig. 31. Even so the predicted pressure variation along the wall did not compare very well with the available experimental data for

this case [36]. In particular, the predicted wall pressure showed a much more rapid rise than that observed experimentally with no plateau which is characteritic of a significant separation region. While the calculation did predict separation, its length and extent was not sufficiently large to modify the wall static pressure distribution significantly.

In the calculation an artificial dissipation parameter of $\sigma = 0.5$ was employed, and all attempts to reduce this value were unsuccessful. It was not known whether the coordinate system, the artificial dissipation or the relatively simple mixing length turbulence model was responsible for the inaccuracies in the predictions. Therefore, a study was undertaken to identify the cause of the discrepancies. First, an oblique shock impinging on a flat plate laminar boundary layer was considered using a mesh similar to that shown in Fig. 30. The case chosen had a freestream Mach number $M = 2.0$, and a shock impinging at an angle of about 32.6 degrees. As in the previous case, the predicted wall pressure rise was more rapid than that observed induced separation region was not as large as that indicated by the experimental skin friction measurements. Also, in this case it was not possible to reduce the artificial dissipation parameter below a value of $\sigma = 0.5$.

Therefore, a calculation was performed for the shock impinging on a laminar boundary layer using a Cartesian grid with 50 transverse points and 100 streamwise points. The computational domain extended from 0.6 inch to 3.1 inches downstream of the plate leading edge, and from 0.0 to 2.0 inches normal to the wall. The inflow boundary layer thickness (.02 inch) for a fully developed turbulent profile was chosen such that the boundary layer velocity profile was reproduced reasonably well at the first data measurement station, 1.1 inches from the plate leading edge. In this case the shock wave impinges at about 1.96 inches, and the shock has little effect on the velocity profile at the first measurement station. The wall pressure distribution for this case is shown in Fig. 32, where it is seen that initial pressure rise begins somewhat upstream of the experimental rise [41] and a plateau longer than that observed experimentally is predicted. The calculation also yielded a separation region extending from about 1.5 to 2.5 inches which is about 0.5 inches longer than the experimental separation region as determined from skin friction meaurements. This larger calculated

separation region is consistent with the longer wall pressure plateau shown in Fig. 32.

In this Cartesian grid calculation an artificial dissipation parameter of $\sigma = 0.5$ was required, and a smooth solution could not be obtained with a smaller value. As a result, the predicted incident and reflected shock waves were excessively smeared even though the calculation utilized a large number of mesh points. Thus, the pressure rise across the shock extended over a larger physical region beginning further upstream than experimentally observed, but with a predicted pressure gradient large enough to cause separation of the laminar boundary layer.

In conclusion, the Cartesian grid calculation of wall pressure for a shock wave impinging on a laminar boundary layer yielded reasonable results with quantitative discrepancies attributable to excessive shock smearing due to artificial dissipation. Modifications to the form and magnitude of the artificial dissipation required for shock capturing are necessary to reduce these errors. Also, shock adapting meshes such as that shown in Fig. 30 should be further investigated because of the potential for sharp shock predictions with a minimum number of mesh points.

## REFERENCES


1. Rehyner, T. and Flugge-Lotz, I.: The Interaction of Shock Waves with a Laminar Boundary Layer. International Journal of Nonlinear Mechanics, Vol. 3, 1968.

2. Briley, W.R. and McDonald, H.: Numerical Prediction of Incompressible Separation Bubbles. Journal of Fluid Mechanics, Vol. 69, 1975, pp. 631-635.

3. Hankey, W.L. and Holden, M.S.: Two-Dimensional Shock Wave Boundary Layer Interactions in HIgh Speed Flows. AGARDograph 203, 1975.

4. MacCormack, R.W.: Numerical Solution of the Interaction of a Shock Wave with a Laminar Boundary Layer. Lecture Notes in Physics, Vol. 8, Springer-Verlag, 1971.

5. MacCormack, R.W. and Baldwin, B.S.: A Numerical Method for Solving the Navier-Stokes Equations with Application to Shock-Boundary Layer Interactions. AIAA Paper No. 75-1, 1975.

6. Deiwert, G.S.: Numerical Simulation of High Reynolds Number Transonic Flows, AIAA Paper No. 74-603, 1971.

7. Baldwin, B.S. and MacCormack, R.W.: Modifications of the Law of the Wall and Algebraic Turbulence Modelling for Separated Boundary Layers. AIAA Paper No. 76-350, 1976.

8. Hung, C.M. and MacCormack, R.W.: Numerical Solutions of Supersonic and Hypersonic Laminar Compression Corner Flows. AIAA Journal, Vol. 14, 1976.

9. Shang, J. and Hankey, W.L.: Numerical Solution of the Navier-Stokes Equations for Supersonic Turbulent Flow Over a Compression Ramp. AIAA Journal, Vol. 13, 1975.

10. Shang, J. and Hankey, W.L.: Numerical Solution of the Compressible Navier-Stokes Equations for a Three-Dimensional Corner. AIAA Paper No. 77-169, 1977.

11. MacCormack, R.W.: An Efficient Numerical Method for Solving the Time-Dependent Compressible Navier-Stokes Equations at High Reynolds Numbers. NASA TM X-73129, 1976.

12. Viegas, J.R. and Coakley, T.J.: Numerical Investigation of Turbulence Models for Shock Separated Boundary Layer Flows. AIAA Paper 77-44, 1977.

13. Levy, R., Shamroth, S.J., Gibeling, H.J. and McDonald, H.: A Study of the Turbulent Shock Wave Boundary Layer Interaction. Air Force Flight Dynamics Laboratory Report AFFDL-TR-76-163, February 1977.

14. Beam, R. and Warming, R.F.: An Implicit Factored Scheme for the Compressible Navier-Stokes Equations. AIAA Paper No. 77-645, 1977

15. Briley, W.R. and McDonald, H.: Solution of the Multidimensional Compressible Navier-Stokes Equations by a Generalized Implicit Method. J. Comp. Physics, Vol. 24, No. 4, August 1977, p. 372.

16. Briley, W.R. and McDonald, H.: On the Structure and Use of Linearized Block Implicit Schemes. J. of Computational Physics, Vol. 34, 1980, pp. 54-73.

17. Bradshaw, P. and Ferriss, D.H.: Calculation of Boundary-Layer Development Using the Turbulent Energy Equation: Compressible Flow on Adiabatic Walls. J. Fluid Mechanics, Vol. 46, Part 1, 1971, pp. 83-110.

18. Launder, B.E. and Spalding, D.B.: The Numerical Computation of Turbulent Flows. Computer Methods in Applied Mechanics and Engineering, Vol. 3, 1974.

19. Gibeling, H.J., Buggeln, R.C. and McDonald, H.: Development of a Two-Dimensional Implicit Interior Ballistics Code, U.S. Army Armament Research and Development Command, Ballistic Research Laboratory Report ARBRL-CR-00411, January 1980.

20. Jones, W.P. and Launder, B.E.: The Prediction of Laminarization with a Two-Equation Model of Turbulence. Int. J. Heat Mass Transfer, Vol. 15, 1972.

21. Shamroth, S.J. and Gibeling, H.J.: A Compressible Solution of the Navier-Stokes Equations for Turbulent Flow About an Airfoil, NASA CR-3183, 1979.

22. McDonald, H. and Fish, R.W.: Practical Calculation of Transitional Boundary Layers. Int. J. Heat and Mass Transfer, Vol. 16, No. 9, 1973, pp. 1729-1744.

23. Shamroth, S.J. and McDonald, H.: Assessment of a Transitional Boundary Layer Theory at Low Hypersonic Mach Numbers. Int. J. Heat and Mass Transfer, Vol. 18, 1975, pp. 1277-1284.

24. Kreskovsky, J.P., Shamroth, S.J. and McDonald, H.: Application of a General Boundary Layer Analysis to Turbulent Boundary Layers Subjected to Strong Favorable Pressure Gradients. J. Fluid Eng., Vol. 97, June 1974, pp. 217-224.

25. Thompson, J.F., Warsi, Z.U.A. and Mastin, C.W.: Boundary-Fitted Coordinate Systems for Numerical Solution of Partial Differential Equations - A Review. J. Comp. Physics, Vol. 47, 1982.

26. Thompson, J.F., Thames, F.C. and Mastin, C.W.: Automatic Numerical Generation of Body-Fitted Curvilinear Coordinate Systems for Fields Containing any Number of Arbitrary Two-Dimensional Bodies. J. Comp. Physics, Vol. 15, 1974.

27. Moretti, G.: Grid Generation Using Classical Techniques. POLY M/AE Report No. 89-25, 1980.

28. Eiseman, P.R.: A Coordinate System for a Viscous Transonic Cascade Analysis. J. Comp. Physics, Vol. 26, 1978.

29. Thomas, P.D. and Lombard, C.K.: Geometric Conservation Law and its Application to Flow Computations on Moving Grids, AIAA Journal, Vol. 17, No. 10, pp. 1030-1037, 1979.

30. Mateer, G.G., Brosh, A., and Viegas, J.R.: A Normal Shock-Wave Turbulent Boundary Layer Interaction at Transonic Speeds, AIAA Paper 76-161, 1976.

31. Roberts, G.O.: Computational Methods for Boundary Layer Problems Proc. of 2nd Int. Conf. on Numerical Methods in Fluid Dynamics, Springer-Verlag, New York, 1971.

32. Johnson, D.A., Horstman, C.C., and Bachalo, W.D.: Comparison Between Experiment and Prediction for a Transonic Turbulent Separated Flow. AIAA J., Vol. 20, No. 6, June 1982.

33. Briley, W.R. and McDonald, H.: Computation of Three-Dimensional Horseshoe Vortex Flow Using the Navier-Stokes Equations. Paper presented at Seventh International Conference on Numerical Methods in Fluid Dynamics, 1980.

34. Cebeci, T., and Smith, A.M.O.: Analysis of Turbulent Boundary Layers, Academic Press, New York, 1974.

35. Wilcox, D.C., nd Rubesin, M.W.: Progress in Turbulence Modeling for Complex Flow Fields, Including Effects of Compressibility, NASA TP-1517, April 1980.

36. Shang, J.S., Hankey, W.L. and Law, C.H.: Numerical Simulation of Shock Wave Turbulent Boundary Layer Interaction, AIAA Paper No. 76-00829, AIAA 14th Aerospace Sciences Meeting, Washington, DC, January 1976.

37. Douglas, J. and Gunn, J.E.: A General Formulation of Alternating Direction Methods. Numerische Math., Vol. 6, pp. 428-453, 1964.

38. Beam, R.M. and Warming, R.F.: An Implicit Factored Scheme for the Compressible Navier-Stokes Equations. AIAA Journal, Vol. 16, pp. 393-402, 1978.

39. Beam, R.M. and Warming, R.F.: An Implicit Finite-Difference Algorithm for Hyperbolic Systems in Conservation-Law Form. J. Comp. Physics, Vol. 22, pp. 87-110, 1976.

40. Patel, V.C., Rodi, W. and Scheurer, G.: Evaluation of Turbulence Models for Near-Wall and Low-Reynolds Number Flows, 3rd Symposium on Turbulent Shear Flows, University of California, Davis, Sept. 1983.

41. Hakkinen, R.J., Greber, I., Trilling, L., Abarbanel, S.S.: The Interaction of an Oblique Shock Wave with a Laminar Boundary Layer, NASA Memorandum 2-18-59W, 1959.

42. Shamroth, S.J., McDonald, H., Briley, W.R.: Prediction of Cascade Flow Fields Using the Averaged Navier-Stokes Equations, J. of Eng. for Gas Turbines and Power, Vol. 106, April 1984, p. 383.

## APPENDIX - SOLUTION PROCEDURE [17]

### Background

The solution procedure employs a consistently-split linearized block implicit (LBI) algorithm which has been discussed in detail in [15, 16]. There are two important elements of this method:

(1) the use of a noniterative formal time linearization to produce a fully-coupled linear multidimensional scheme which is written in "block implicit" form; and

(2) solution of this linearized coupled scheme using a consistent "splitting" (ADI scheme) patterned after the Douglas-Gunn [37] treatment of scalar ADI schemes.

The method is thus referred to as a split linearized block implicit (LBI) scheme. The method has several attributes:

(1) the noniterative liearization is efficient;

(2) the fully-coupled linearized algorithm eliminates instabilities and/or extremely slow convergence rates often attributed to methods which employ ad hoc decoupling and linearization assumptions to identify nonlinear coefficients which are then treated by lag and update techniques;

(3) the splitting or ADI technique produces an efficient algorithm which is stable for large time steps and also provides a means for convergence acceleration for further efficiency in computing steady solutions;

(4) intermediate steps of the splitting are consistent with the governing equations, and this means that the "physical" boundary conditions can be used for the intermediate solutions. Other splittings which are inconsistent can have several difficulties in satisfying physical boundary conditions [16].

(5) the convergence rate and overall efficiency of the algorithm are much less sensitive to mesh refinement and redistribution than algorithms based on explicit schemes or which employ ad hoc decoupling and linearization assumptions. This is important for accuracy and for computing turbulent flows with viscous sublayer resolution; and

(6) the method is general and is specifically designed for the complex systems of equations which govern multiscale viscous flow in complicated geometries.

This same algorithm was later considered by Beam and Warming [38], but the ADI splitting was derived by approximate factorization instead of the Douglas-Gunn procedure. They refer to the algorithm as a "delta form" approximate factorization scheme. This scheme replaced an earlier non-delta form scheme [39], which has inconsistent intermediate steps.

## Split LBI Algorithm

### Linearization and Time Differencing

The system of governing equations to be solved consists of three/four equations: continuity and two/three components of momentum equation in three/four dependent variables: $\rho$, u, v, w. Using notation similar to that in [15], at a single grid point this system of equations can be written in the following form:

$$\partial H(\phi)/\partial t = D(\phi) + S(\phi) \tag{1}$$

where $\phi$ is the column-vector of dependent variables, H and S are column-vector algebraic functions of $\phi$, and D is a column vector whose elements are the spatial differential operators which generate all spatial derivatives appearing in the governing equation associated with that element.

The solution procedure is based on the following two-level implicit time-difference approximations of (3):

$$(H^{n+1} - H^n)/\Delta t = (D^{n+1}) + (1-\beta)\,(D^n + S^n) \tag{2}$$

where, for example, $H^{n+1}$ denotes $H(\phi^{n+1})$ and $\Delta t = t^{n+1} - t^n$. The parameter $\beta$ $(0.5 \le \beta \le 1)$ permits a variable time-centering of the scheme, with a truncation error of order $[\Delta t^2, (\beta - 1/2)\,\Delta t]$.

A local time linearization (Taylor expansion about $\phi^n$) of requisite formal accuracy is introduced, and this serves to define a <u>linear</u> differential operator L (cf. [15]) such that

$$D^{n+1} = D^n + L^n(\phi^{n+1} - \phi^n) + O(\Delta t^2) \tag{3}$$

Similarly,

$$H^{n+1} = H^n + (\partial H/\partial \phi)^n (\phi^{n+1} - \phi^n) + 0 (\Delta t^2) \quad (4)$$

$$S^{n+1} = S^n + (\partial S/\partial \phi)^n (\phi^{n+1} - \phi^n) + 0 (\Delta t^2) \quad (5)$$

Eqs. (5-7) are inserted into Eq. (4) to obtain the following system which is linear in $\phi^{n+1}$

$$(A - \beta \Delta t\, L^n) (\phi^{n+1} - \phi^n) = \Delta t (D^n + S^n) \quad (6)$$

and which is termed a linearized block implilcit (LBI) scheme. Here, A denotes a matrix defined by

$$A \equiv (\partial H/\partial \phi)^n - \beta \Delta t (\partial S/\partial \phi)^n \quad (7)$$

Eq. (8) has 0 ($\Delta t$) accuracy unless $H \equiv \phi$, in which case the accuracy is the same as Eq. (4).

Special Treatment of Diffusive Terms

The time differencing of diffusive terms is modified to accomodate cross-derivative terms and also turbulent viscosity and artificial dissipation coefficients which depend on the solution variables. Although formal linearization of the convection and pressure gradient terms and the resulting implicit coupling of variables is critical to the stability and rapid convergence of the algorithm, this does not appear to be important for the turbulent viscosity and artificial dissipation coefficients. Since the relationship between $\mu_e$ and $d_j$ and the mean flow variables is not conveniently linearized, these diffusive coefficients are evaluated explicitly at $t^n$ during each time step. Notationally, this is equivalent to neglecting terms proportional to $\partial\, \mu_e/\partial\phi$ or $\partial d_j/\partial\phi$ in $L^n$, which are formally present in the Taylor expansion (5), but retaining all terms proportional to $\mu_e$ or $d_j$ in both $L^n$ and $D^n$.

It has been found through extensive experience that this has little if any effect on the performance of the algorithm. This treatment also has the added benefit that the turbulence model equations can be decoupled from the system of mean flow equations by an appropriate matrix partitioning (cf. [15]) and solved separately in each step of the ADI solution procedure. This reduces the block size of the block tridiagonal systems which must be solved in each step and thus reduces the computational labor.

In addition, the viscous terms in the present formulation include a num cross-derivative terms implicitly within the ADI treatment which follows, it is not at all convenient to do so; and consequently, all cross-derivative

terms are evaluated explicitly at $t^n$. For a scalar model equationrepresenting combined convection and diffusion, it has been shown by Beam and Warming that the explicit treatment of cross-derivative terms does not degrade the unconditional stability of the present algorithm. To preserve notational simplicity, it is understood that all cross-derivative terms appearing in $L^n$ are neglected but are retained in $D^n$. It is important to note that neglecting terms in $L^n$ has no effect on steady solutions of Eq. (8), since $\phi^{n+1} \equiv 0$ and thus Eq. (8) reduces to the steady form of the equations: $D^n + S^n = 0$. Aside from stability considerations, the only effect of neglecting terms in $L^n$ is to introduce an $0(\Delta t)$ truncation error.

Consistent Splitting of the LBI Scheme

To obtain an efficient algorithm, the linearized system (8) is split using ADI techniques. To obtain the split scheme, the multidimensional operator L is rewritten as the sum of three "one-dimensional" sub-operators $L_i$ (i = 1, 2, 3) each of which contains all terms having derivatives with respect to the i-th coordinate. The split form of Eq. (8) can be derived either as in [19, 22] by following the procedure described by Douglas and Gunn [23] in their generalization and unification of scalar ADI schemes, or using approximate factorization. For the present system of equations, the split algorithm is given by

$$(A - \beta\Delta t L_1^n)\,(\phi^* - \phi^n) = \Delta t\,(D^n + S^n) \tag{8a}$$

$$(A - \beta\Delta t L_2^n)\,(\phi^{**} - \phi^n) = A\,(\phi^* - \phi^n) \tag{8b}$$

$$(A - \beta\Delta t L_3^n)\,(\phi^{n+1} - \phi^n) = A\,(\phi^{**} - \phi^n) \tag{8c}$$

where $\phi^*$ and $\phi^{**}$ are consistent intermediate solutions. If spatial derivatives appearing in $L_i$ and D are replace by three-point difference formulas, as indicated previously, then each step in Eqs. (10a-c) can be solved by a block-tridiagonal elimination.

Combining Eqs. (10a-c) gives

$$(A - \beta\Delta t L_1^n)\,A^{-1}\,(A - \beta\Delta t L_2^n)\,A^{-1}\,(A - \beta\Delta t L_3^n)\,(\phi^{n+1} - \phi^n) = \delta t\,(D^n + S^n) \tag{9}$$

which approximates the unsplit scheme (8) to $0(\Delta t^2)$. Since the intermediate steps are also consistent approximations for Eq. (8), physical boundary conditions can be used for $\phi^*$ and $\phi^{**}$ [19, 22]. Finally, since the $L_i$ are homogeneous operators, it follows from Eqs. (10a-c) that steady solutions

have the property that $\phi^{n+1} = \phi^* = \phi^{**} = \phi^n$ and satisfy

$$D^n + S^n = 0 \qquad (10)$$

The steady solution thus depends only on the spatial difference approximations used for (12), and does not depend on the solution algorithm itself.

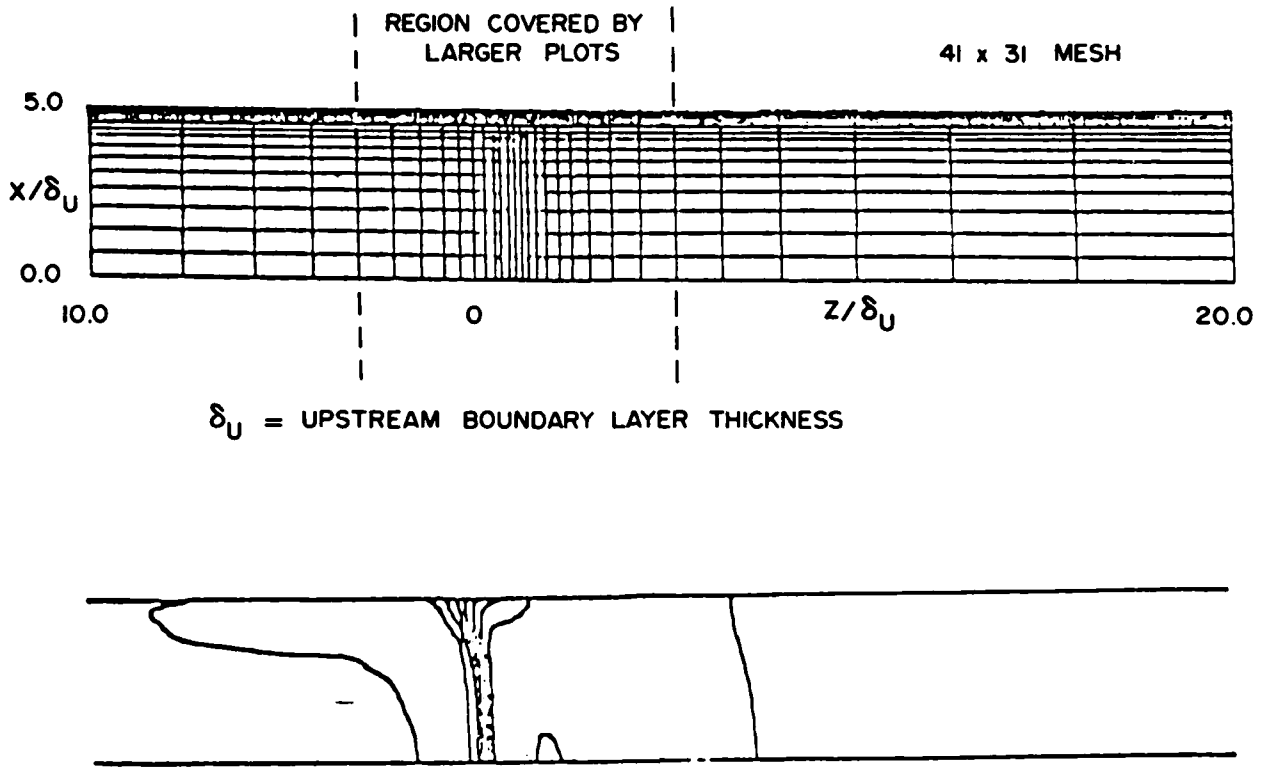


FIGURE 1 — SOLUTION ADAPTIVE COORDINATE SYSTEM SHOWN IN RELATION TO SHOCK LOCATION

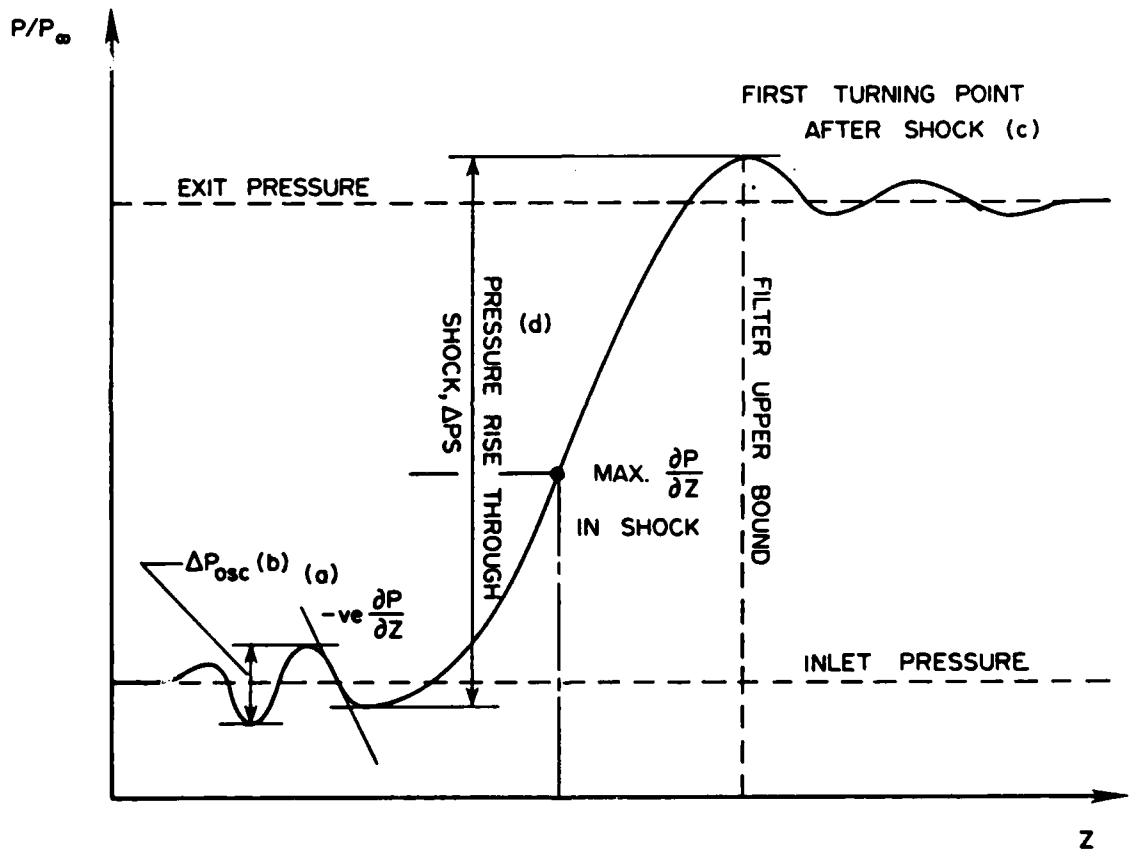


FIGURE 2 – SCHEMATIC REPRESENTATION OF THE ADAPTIVE GRID SHOCK LOCATION PROCEEDURE

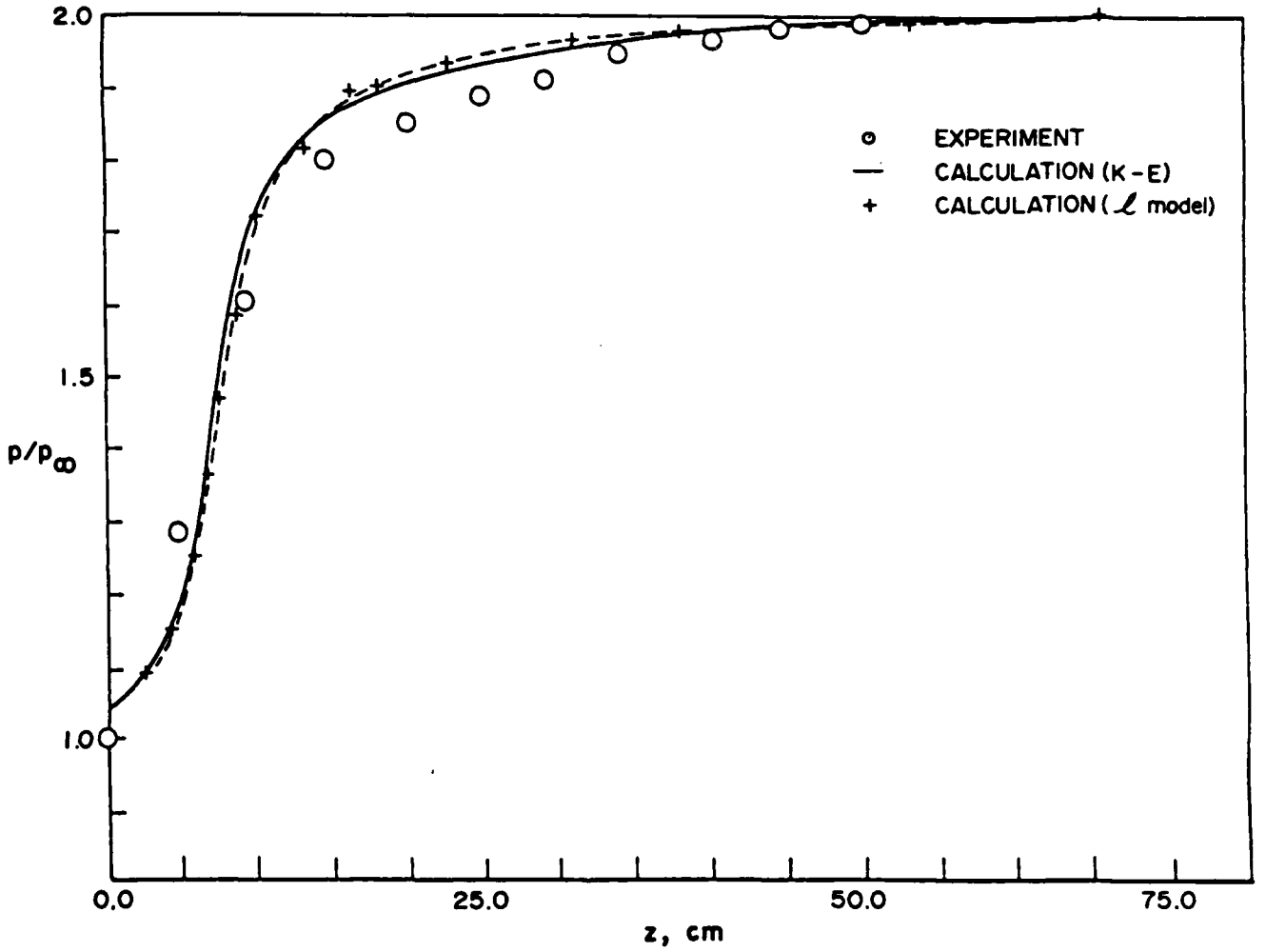


FIGURE 3— WALL STATIC PRESSURE DISTRIBUTION FOR A NORMAL SHOCK IN A TUBE AT $M_\infty = 1.44$

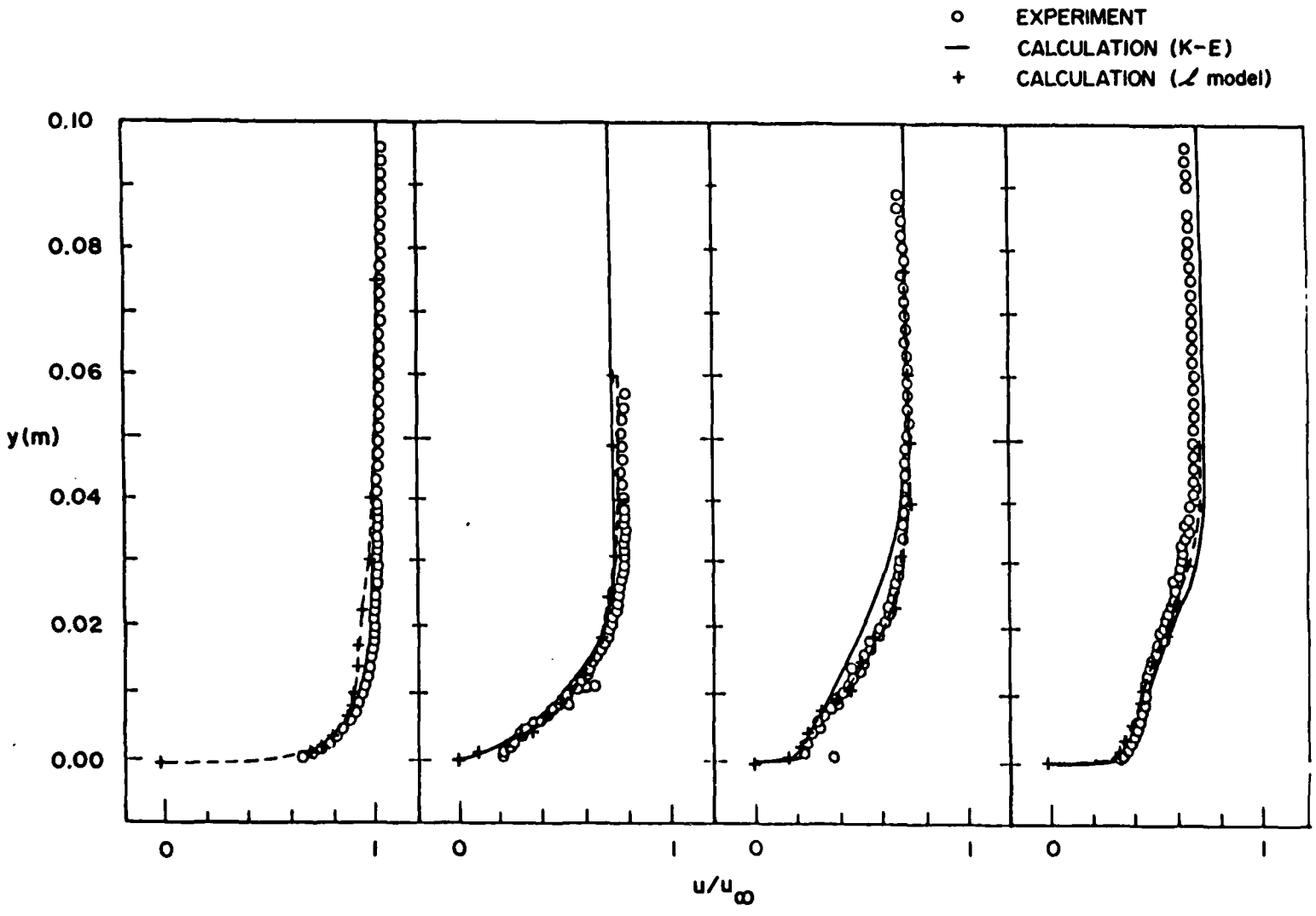


FIGURE 4 – MEAN VELOCITY PROFILE

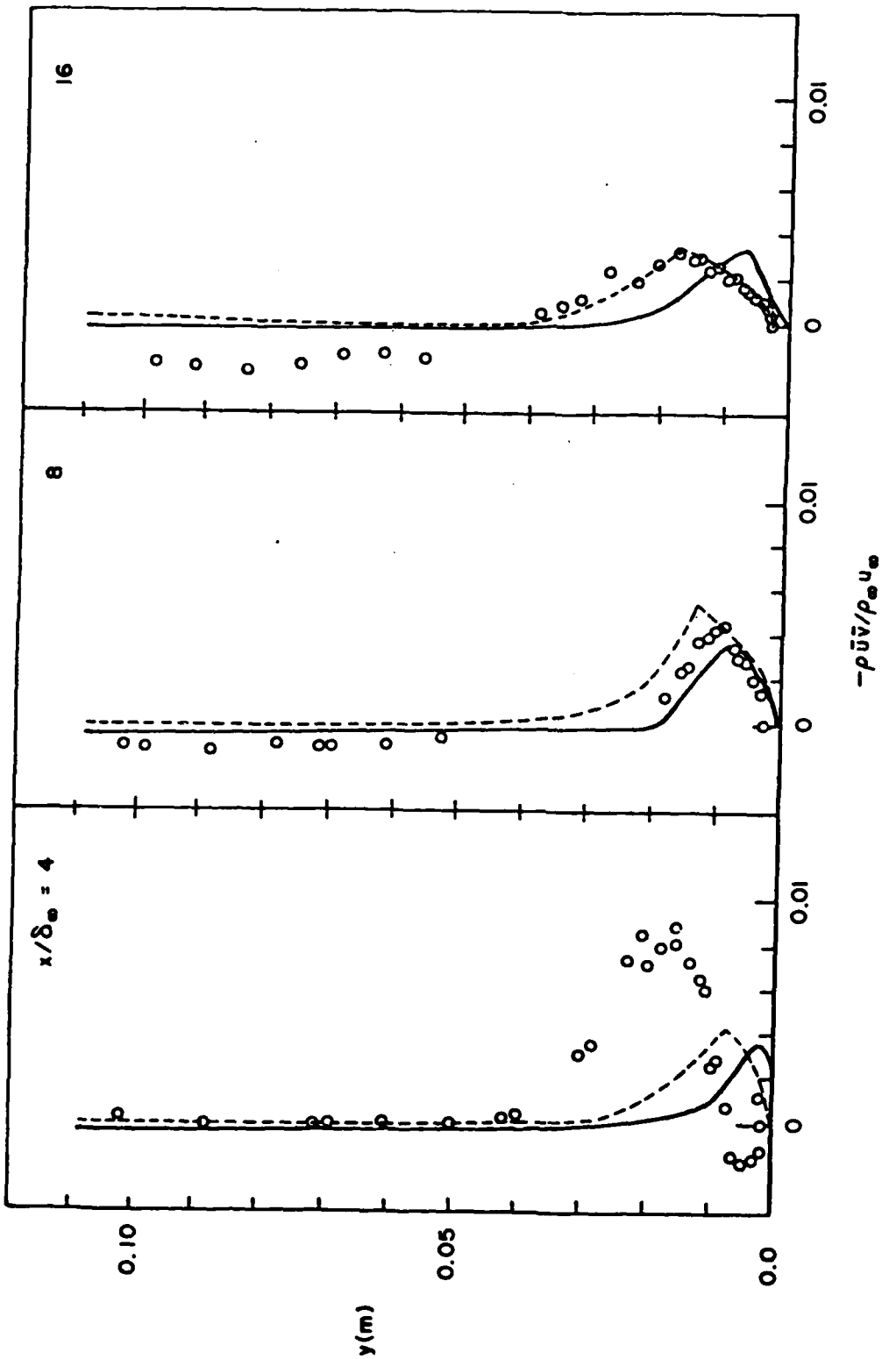


FIGURE 5— REYNOLD'S SHEAR STRESS PROFILE

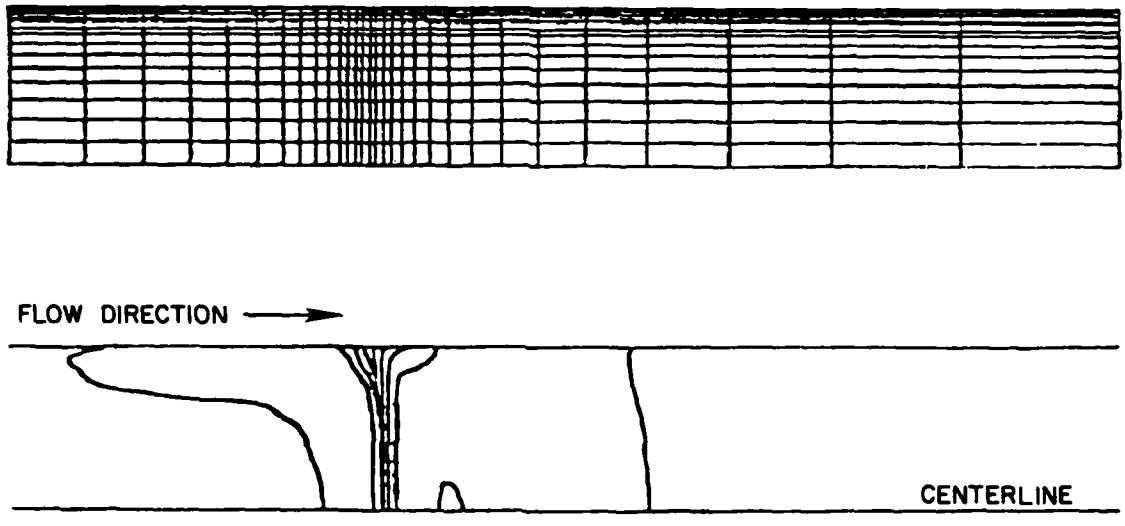


FIGURE 6- CALCULATION COORDINATE SYSTEM AND CONSTANT STATIC PRESSURE CONTOURS FOR THE CONVERGED NORMAL SHOCK WAVE/BOUNDARY LAYER INTERACTION IN A TUBE

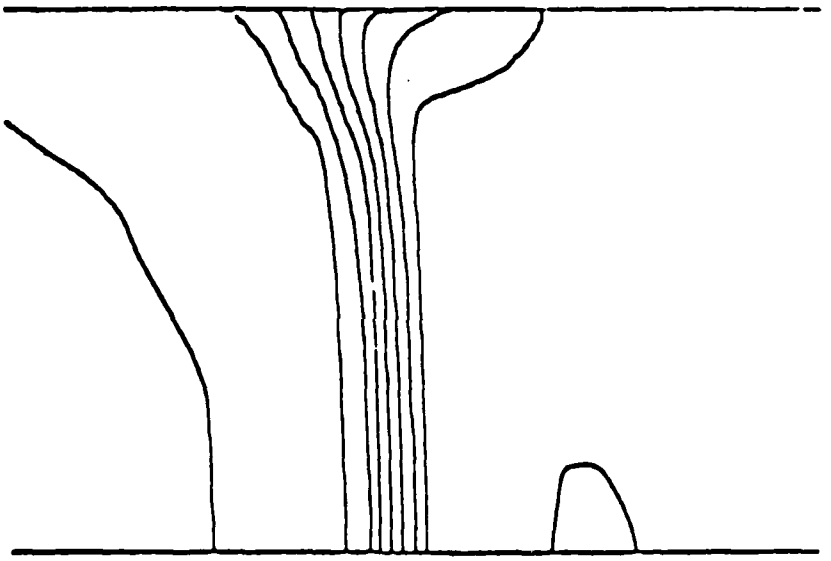

FIGURE 7 – PRESSURE CONTOURS CLOSE TO THE SHOCK

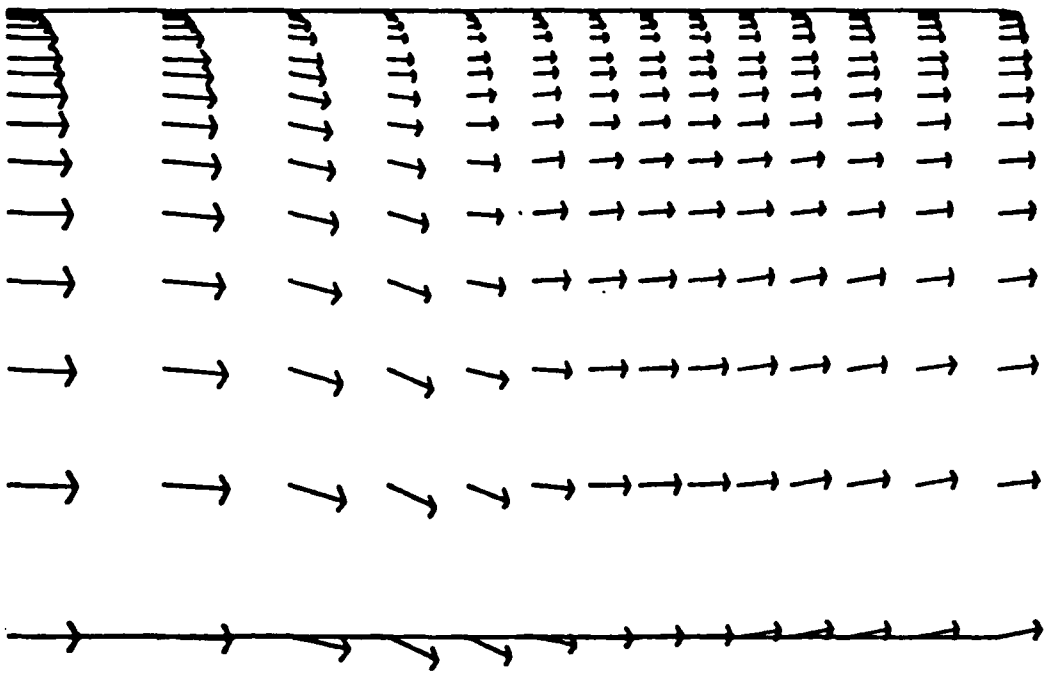

FIGURE 8- VELOCITY VECTORS IN THE NEAR WALL REGION OF THE SHOCK WAVE / BOUNDARY LAYER INTERACTION

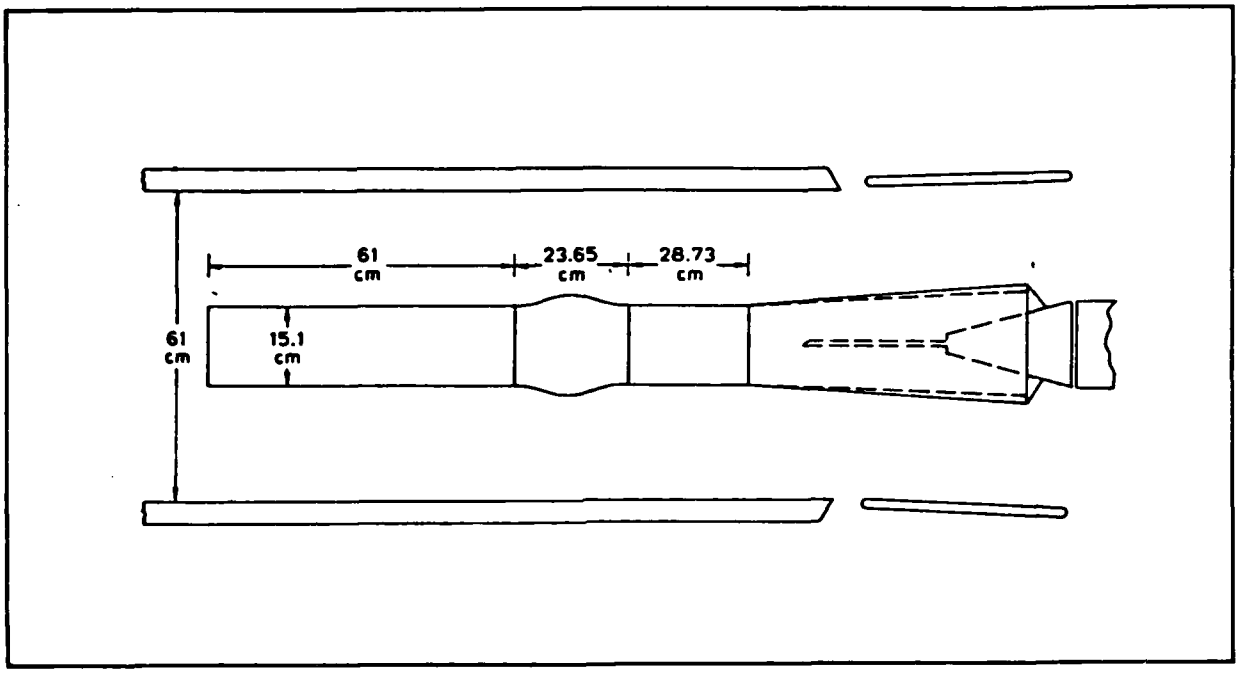


FIGURE 9 — TRANSONIC AXISYMMETRIC BUMP: EXPERIMENTAL ARRANGEMENT

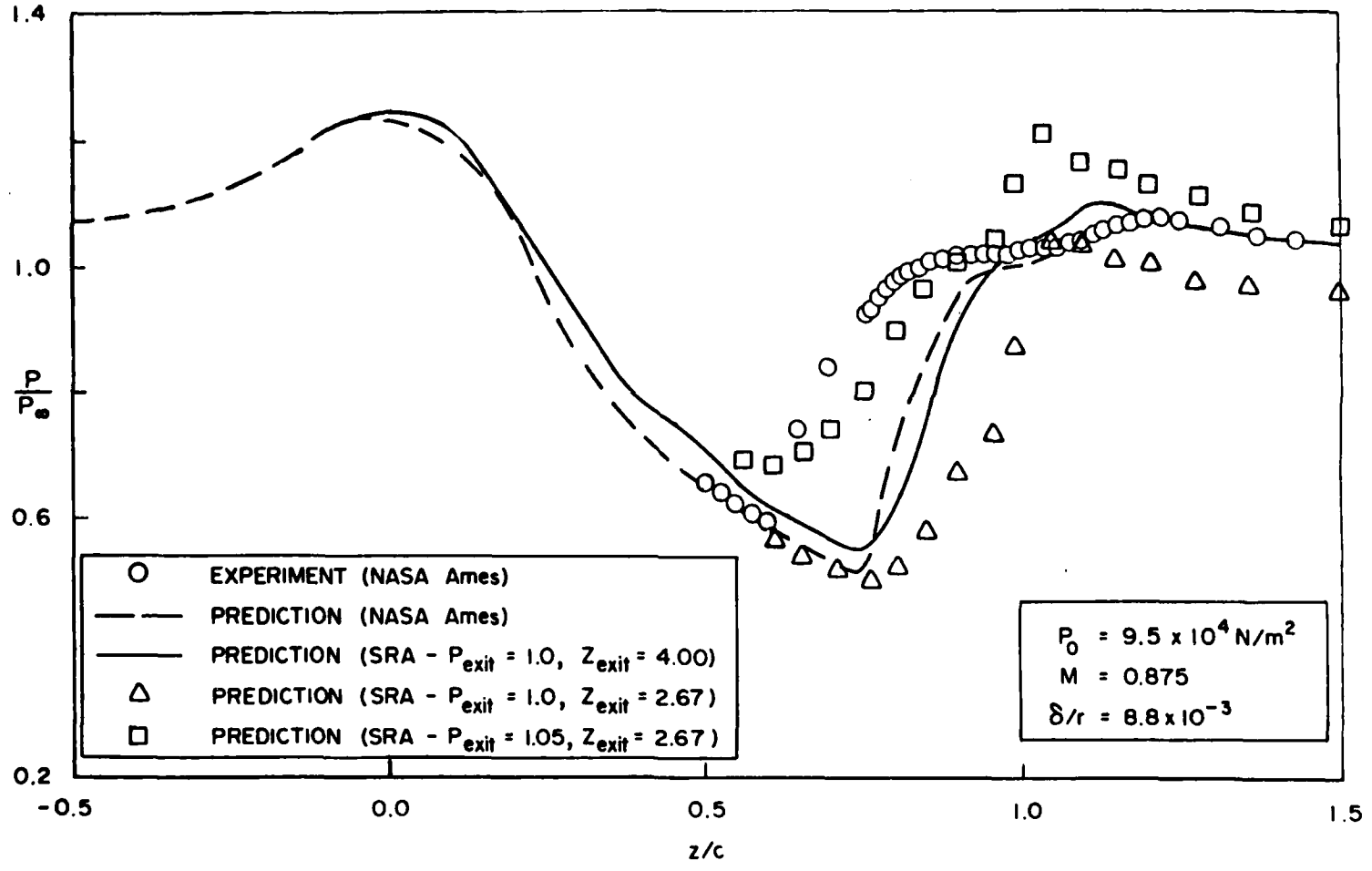


FIGURE 10 — COMPARISON OF PREDICTION AND EXPERIMENT FOR LARGE RADIUS OF CURVATURE BUMP WITH THIN INITIAL BOUNDARY LAYER

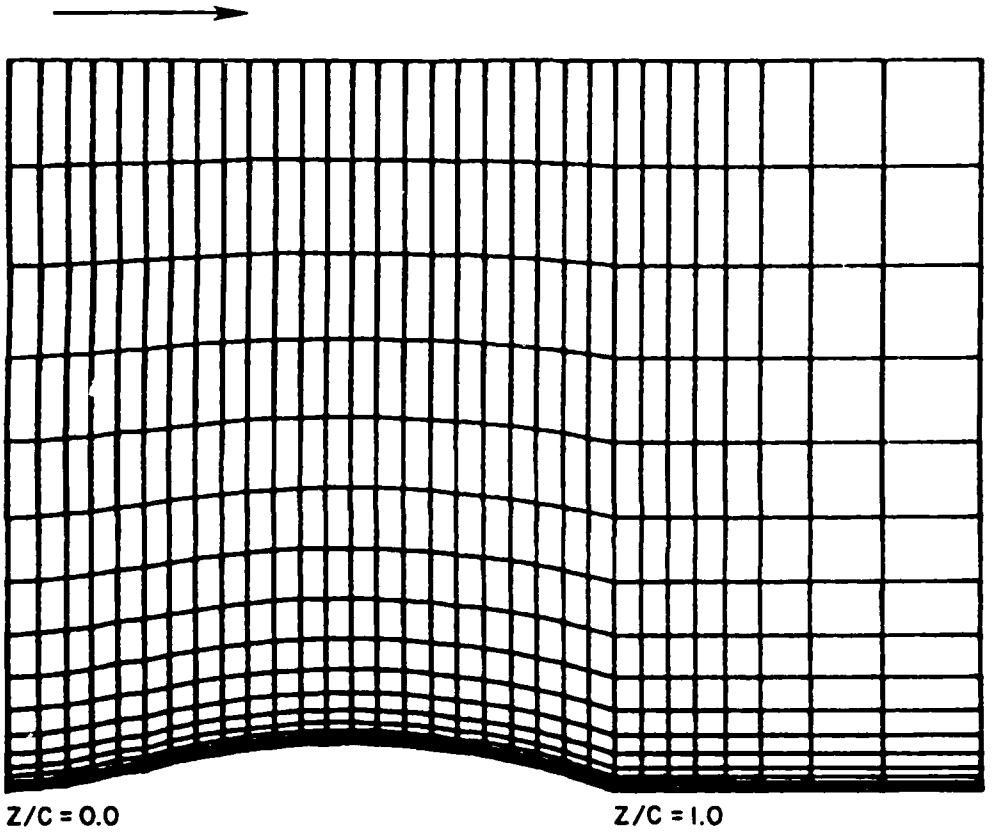


FIGURE 11– PART OF THE COORDINATE SYSTEM FOR THE LARGE RADIUS OF CURVATURE BUMP WITH THIN INLET BOUNDARY LAYER

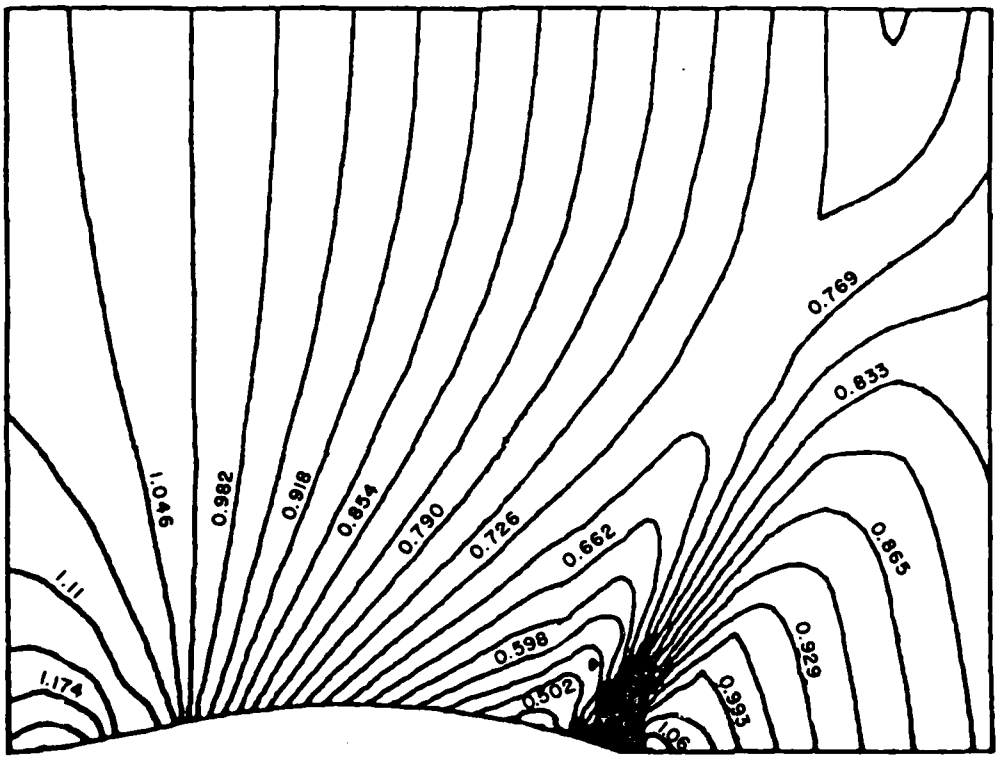


FIGURE 12 – CONSTANT STATIC PRESSURE CONTOURS LARGE RADIUS OF CURVATURE BUMP, THIN APPROACH BOUNDARY LAYER

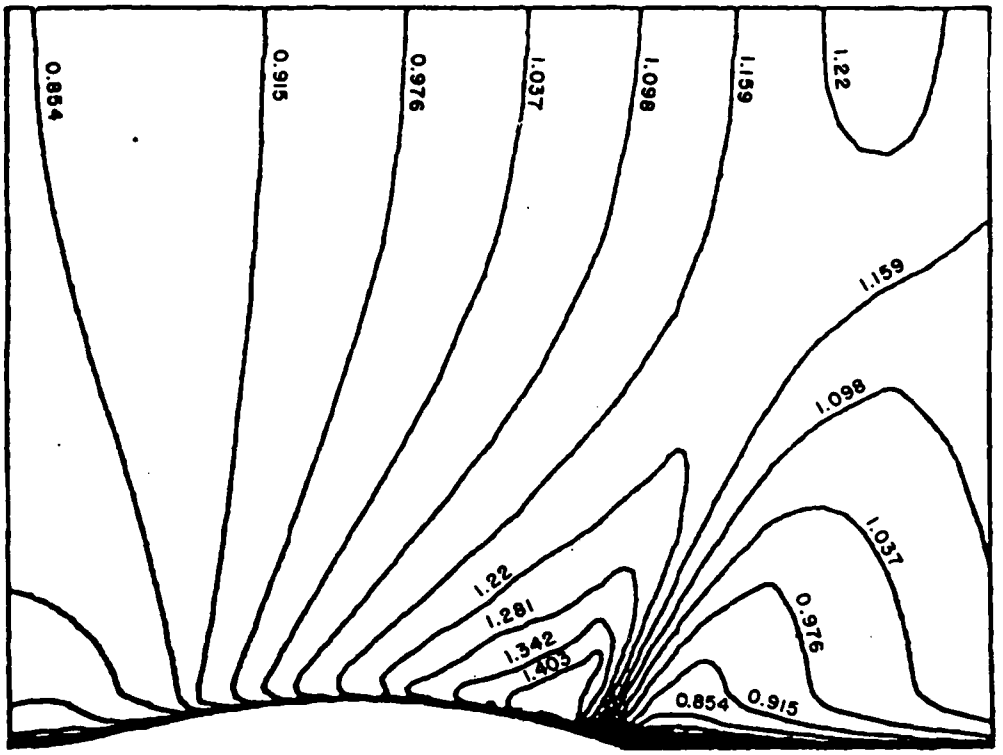


FIGURE 13 — CONSTANT MACH NUMBER CONTOURS: LARGE RADIUS OF CURVATURE BUMP, THIN APPROACH BOUNDARY LAYER

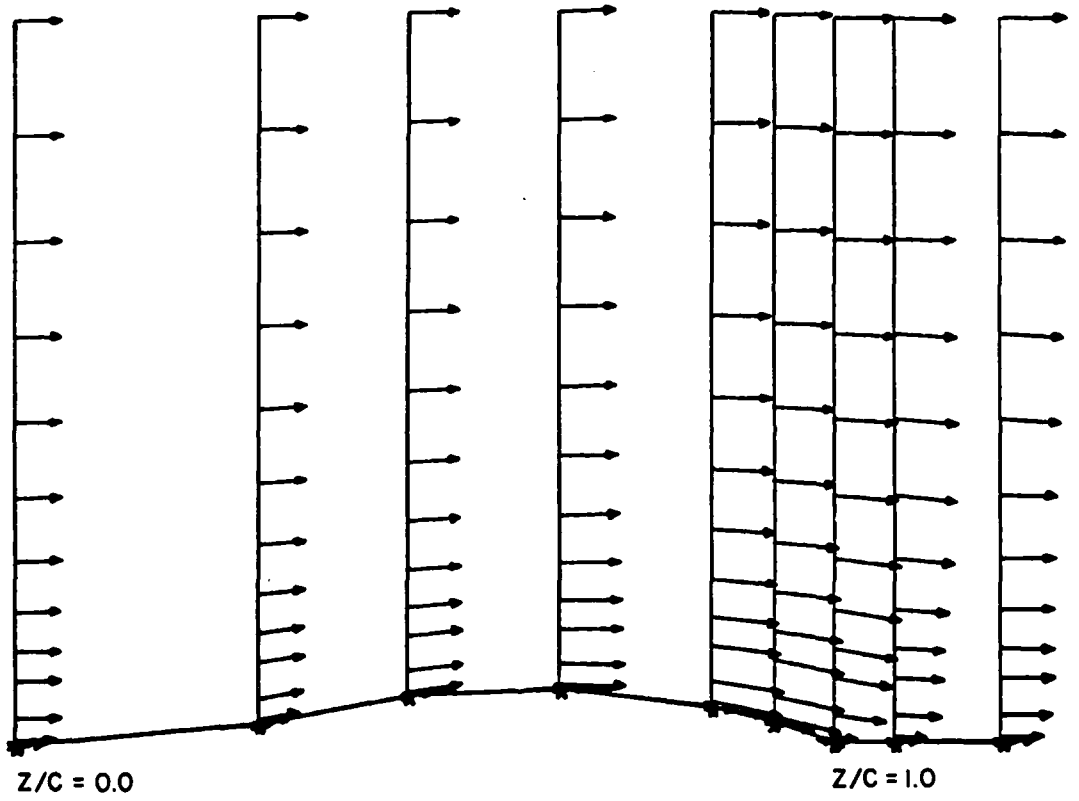


FIGURE 14 – VELOCITY VECTORS: LARGE RADIUS OF CURVATURE BUMP, THIN APPROACH BOUNDARY LAYER

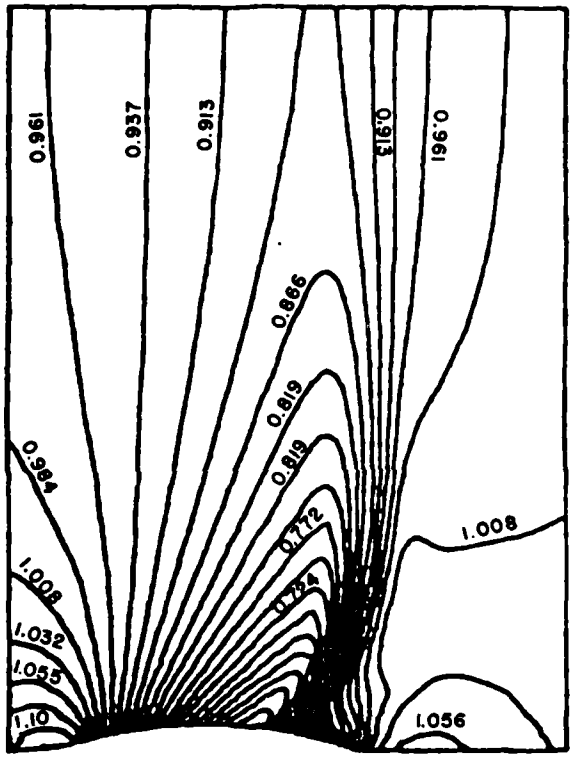


FIGURE 15 — CONSTANT STATIC PRESSURE CONTOURS: LARGE RADIUS OF CURVATURE BUMP, THICK APPROACH BOUNDARY LAYER

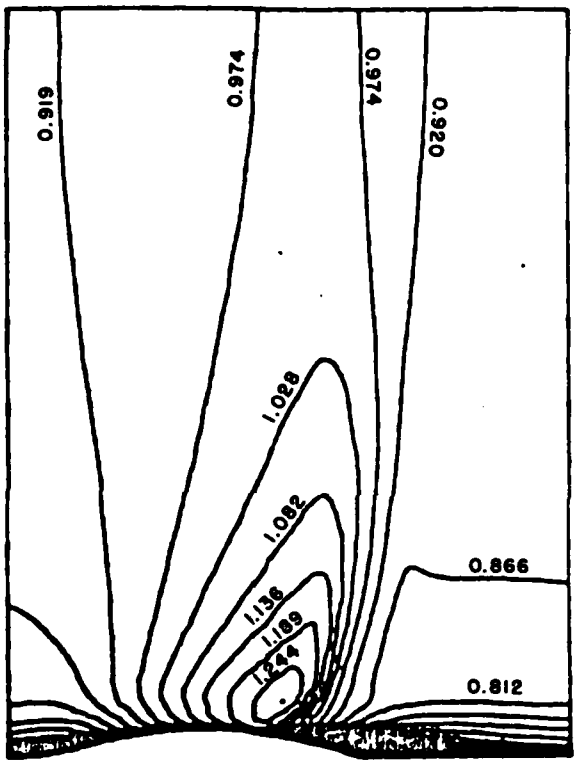


FIGURE 16 — CONSTANT MACH NUMBER CONTOURS: LARGE RADIUS OF CURVATURE BUMP, THICK APPROACH BOUNDARY LAYER

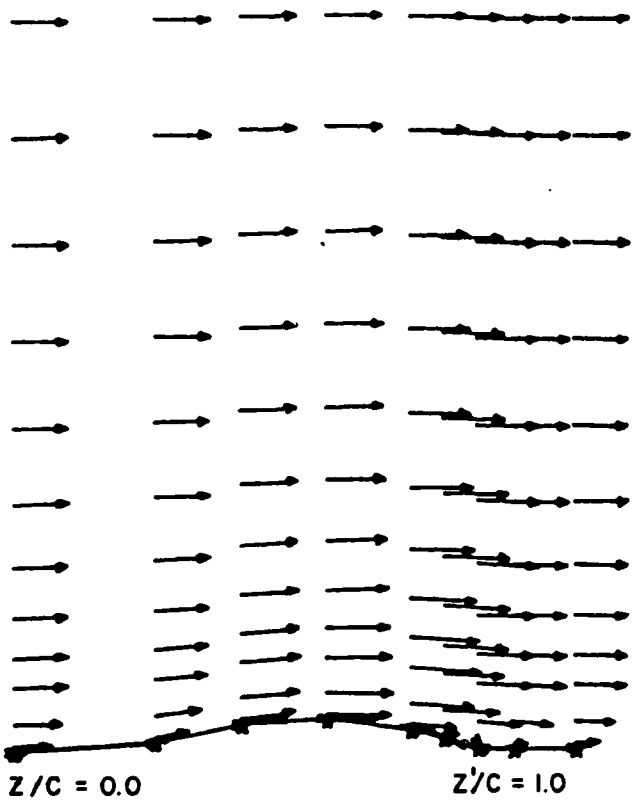


FIGURE 17 – VELOCITY VECTORS: LARGE RADIUS OF CURVATURE BUMP, THICK APPROACH BOUNDARY LAYER

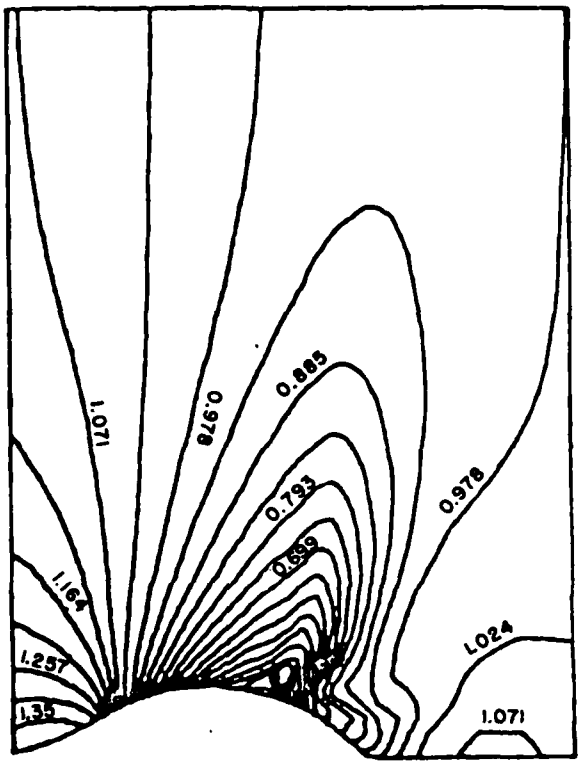


FIGURE 18 — CONSTANT STATIC PRESSURE CONTOURS: SMALL RADIUS OF CURVATURE BUMP, THIN APPROACH BOUNDARY LAYER

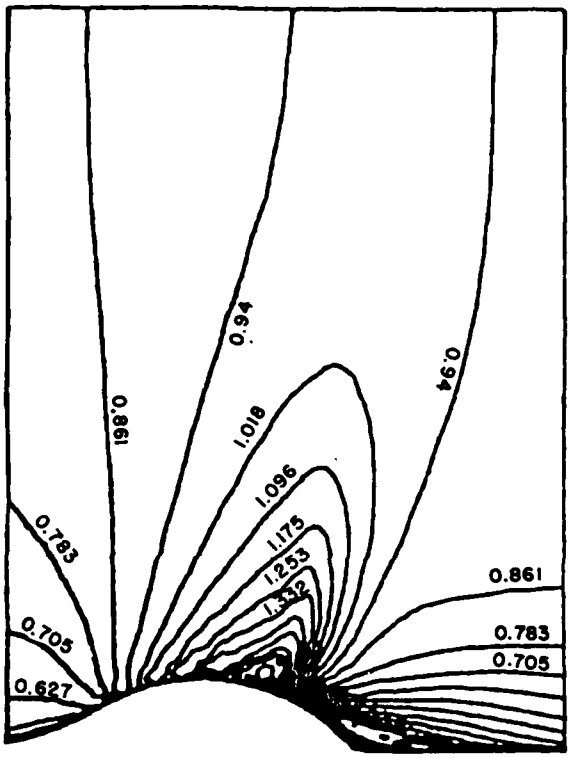


FIGURE 19 – CONSTANT MACH NUMBER CONTOURS: SMALL RADIUS OF CURVATURE BUMP, THIN APPROACH BOUNDARY LAYER

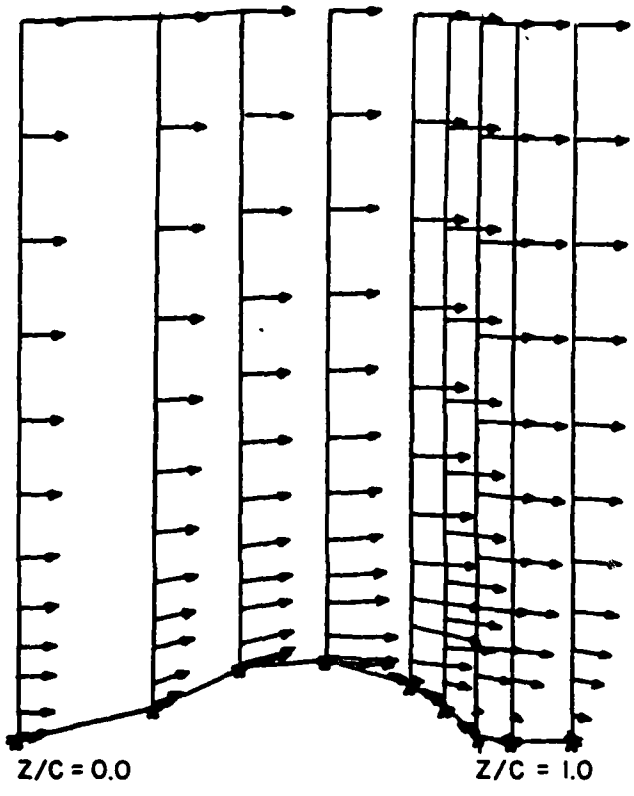


FIGURE 20 – VELOCITY VECTORS: SMALL RADIUS OF CURVATURE BUMP, THIN APPROACH BOUNDARY LAYER

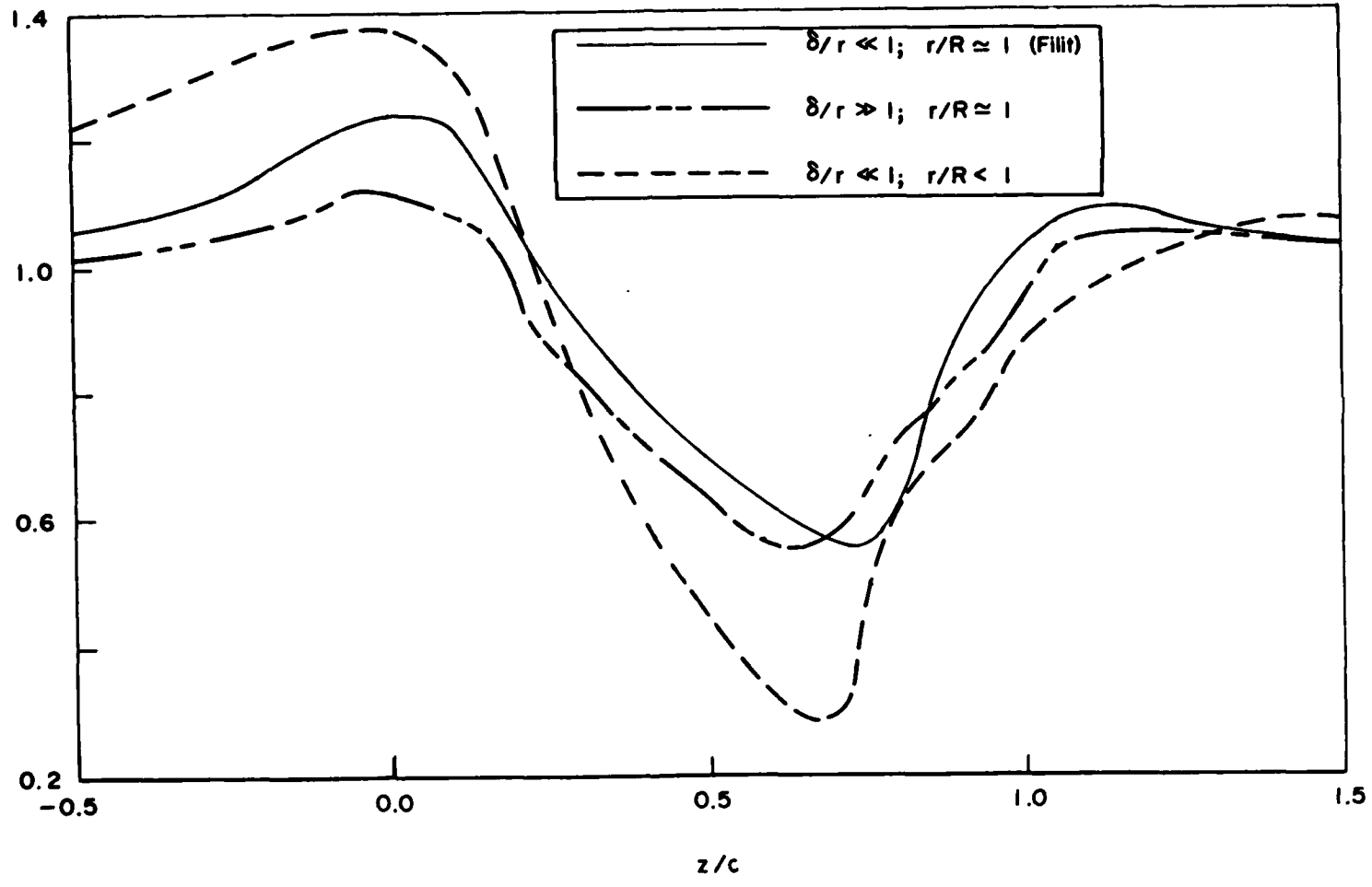


FIGURE 21 – COMPARISON OF WALL PRESSURE DISTRIBUTION FOR EACH CONFIGURATION

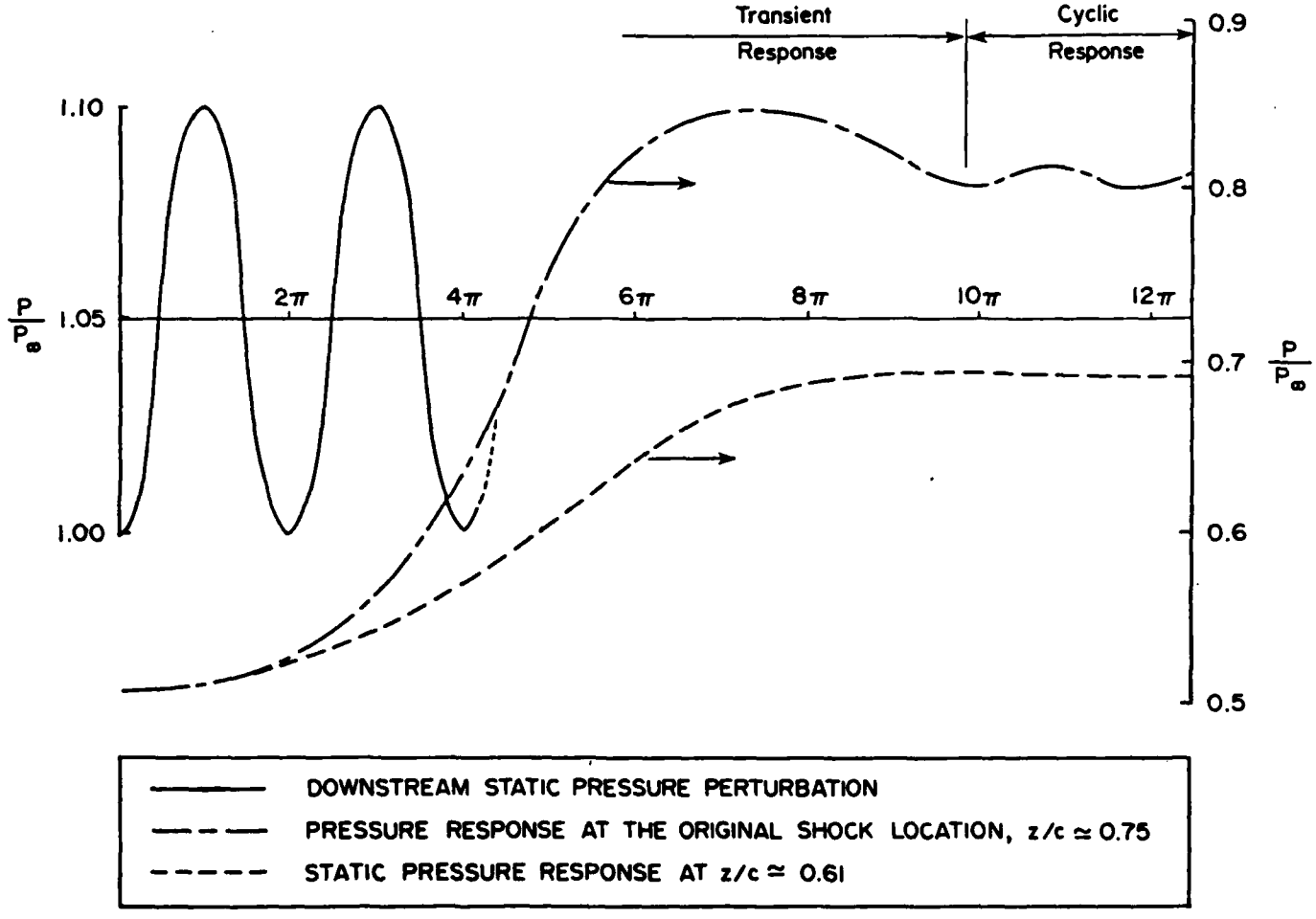


FIGURE 22 – TIME HISTORY OF WALL STATIC PRESSURE FOR TRANSONIC, TURBULENT FLOW OVER AN AXISYMMETRIC BUMP AT REDUCED FREQUENCY ($f_r$ = .0.175)

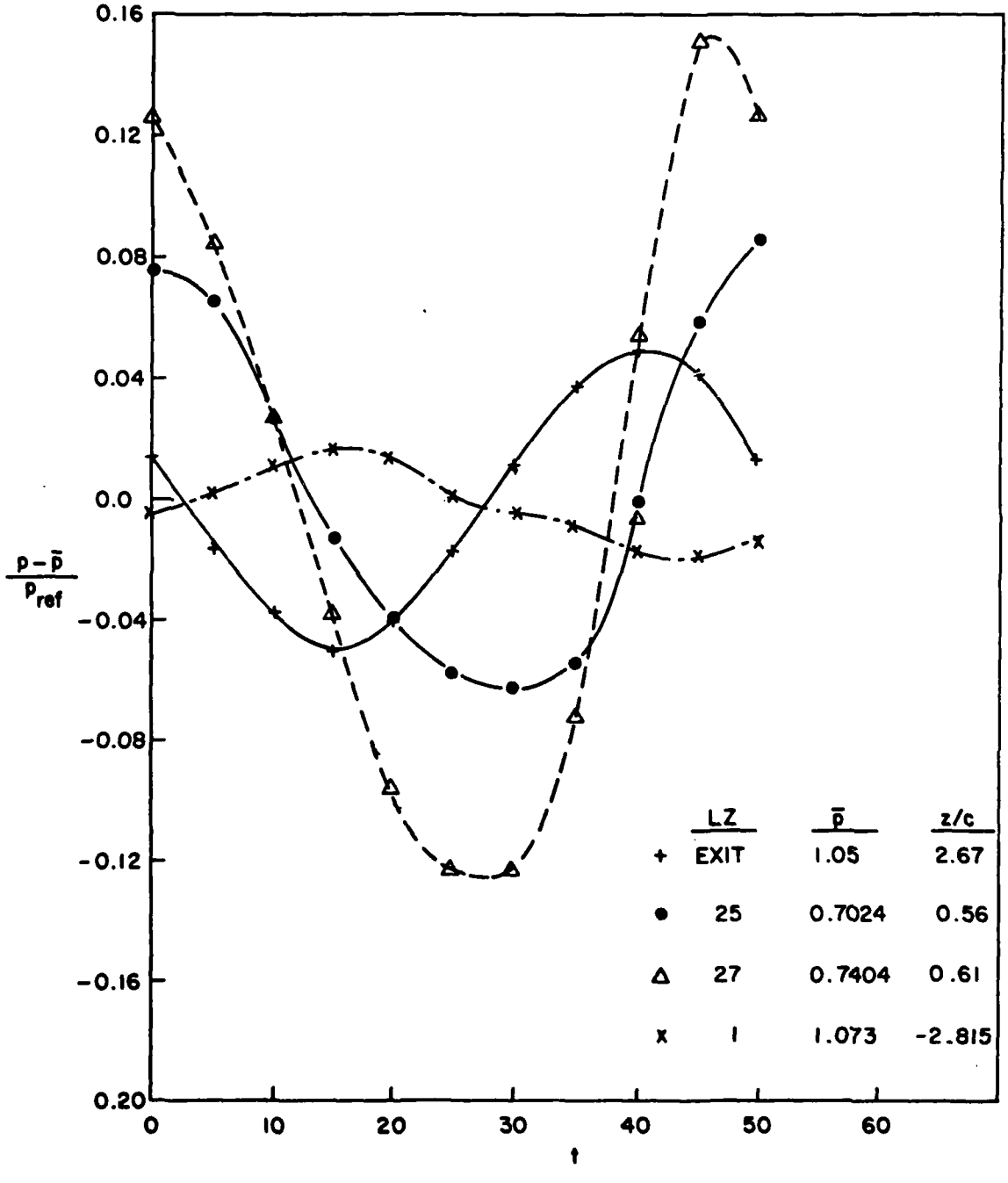


FIGURE 23 – FREQUENCY RESPONCE FOR UNSTEADY FLOW OVER AN AXISYMMETRIC BUMP ($f_r = 0.004$).

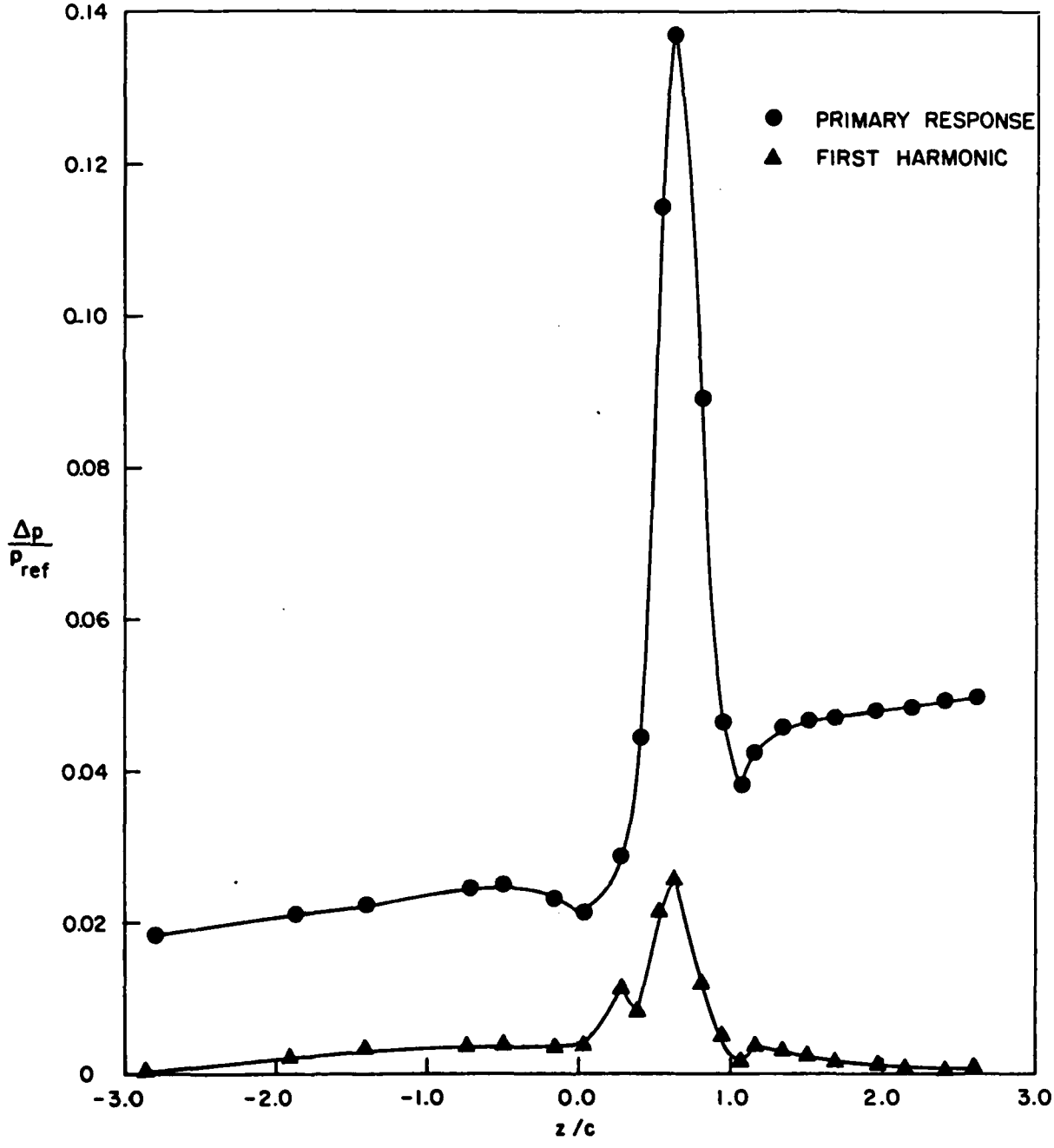


FIGURE 24 - DISTRIBUTION OF AMPLITUDE OF PRIMARY AND FIRST HARMONIC OF THE RESPONSE TO UNSTEADY EXIT PRESSURE PERTURBATIONS ($f_r$ = 0.004)

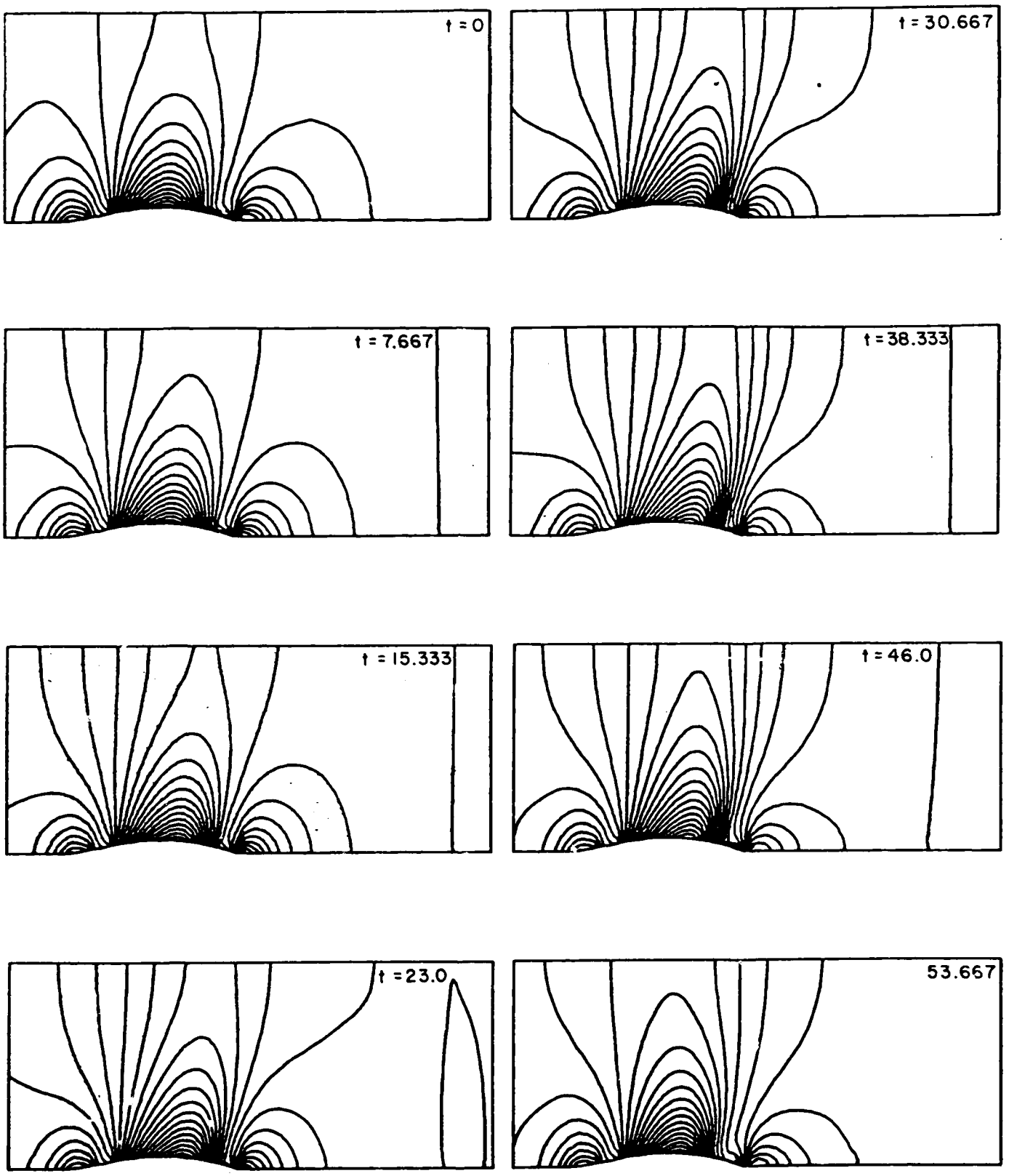


FIGURE 25— TIME HISTORY OF CONSTANT STATIC PRESSURE CONTOURS FOR AXISYMMETRIC BUMP FLOW SUBJECT TO OSCILLATING DOWNSTREAM PRESSURE

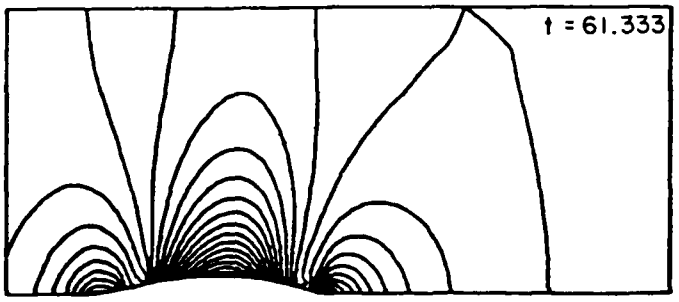


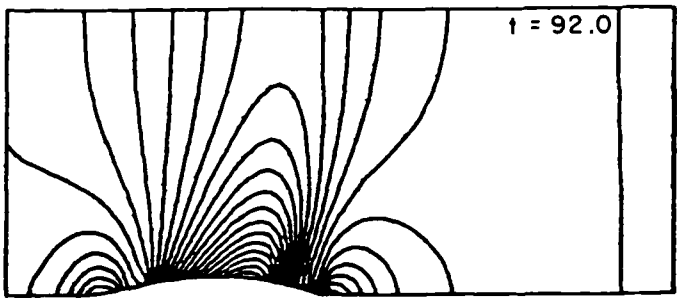


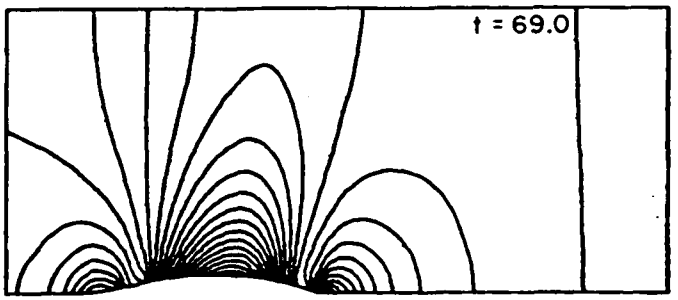


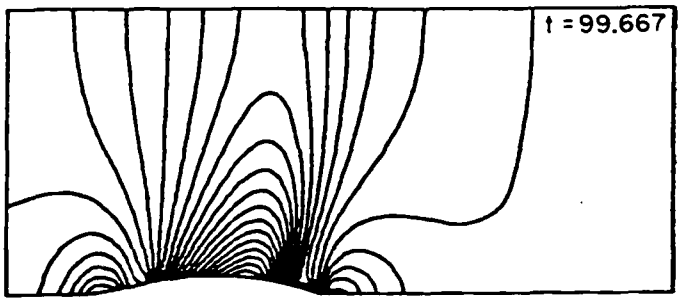


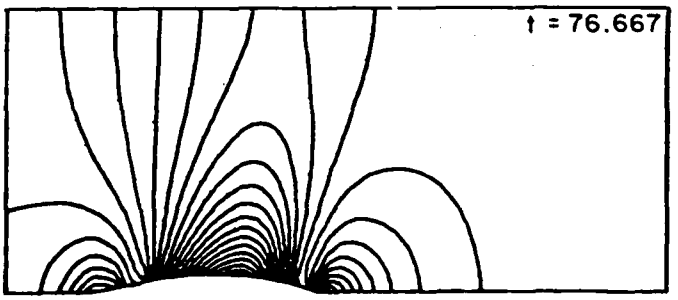


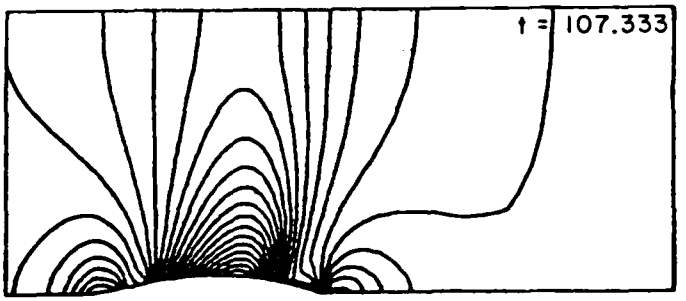


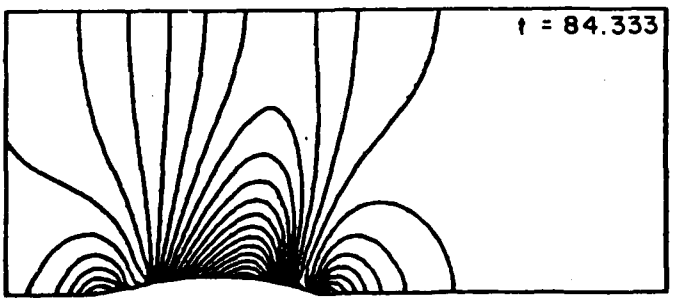


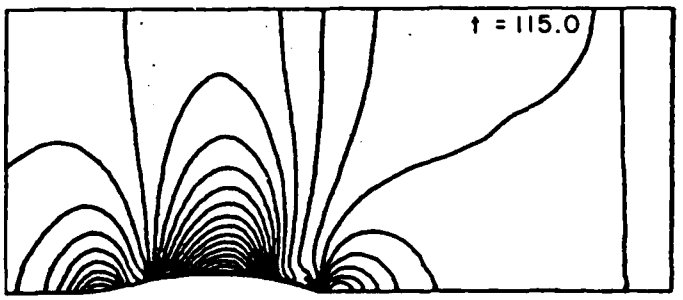


FIGURE 25- (continued)

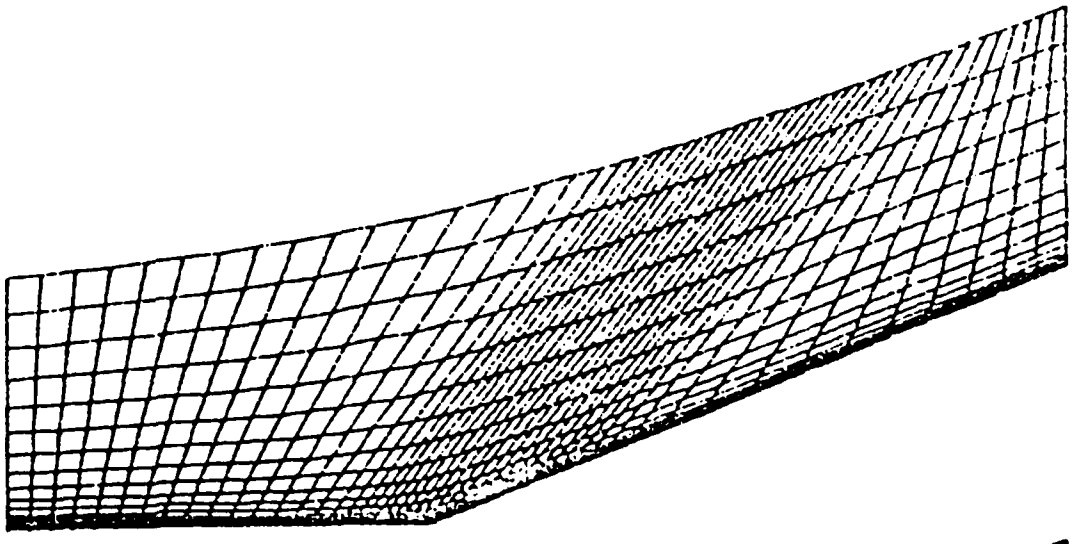

FIGURE 26 — COMPRESSION RAMP: COORDINATE SYSTEM

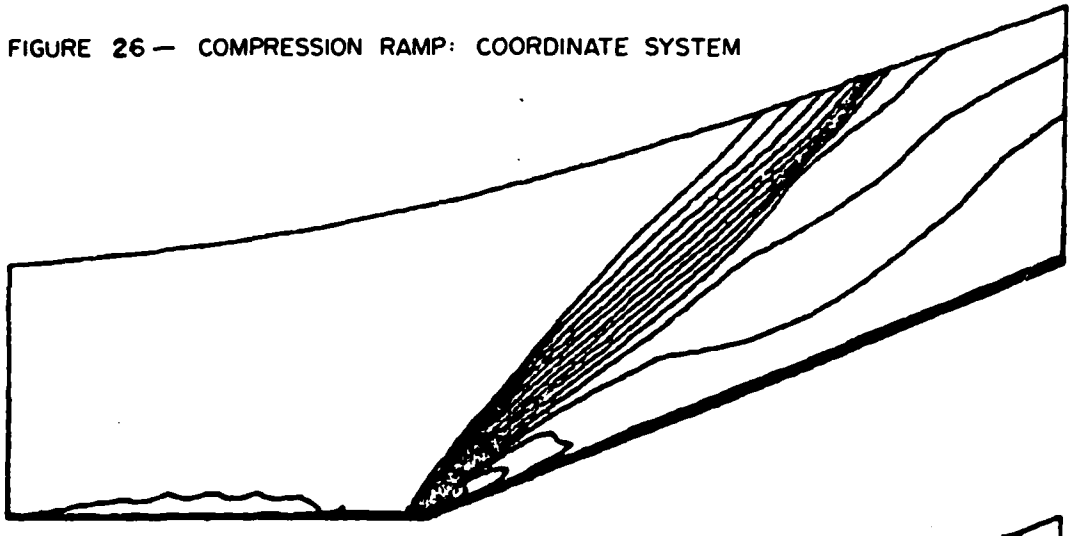

FIGURE 27 — COMPRESSION RAMP: DENSITY CONTOURS

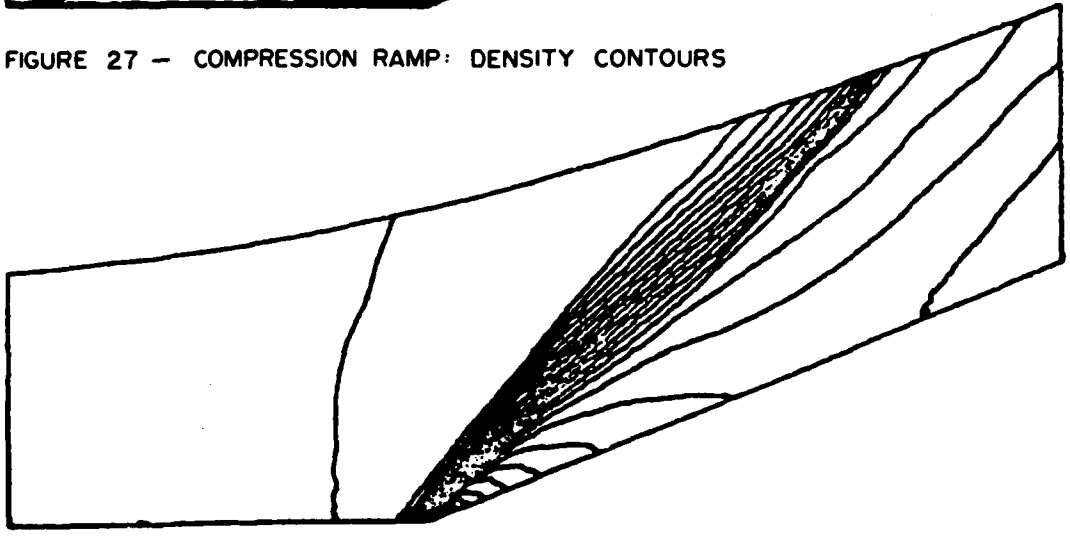

FIGURE 28 — COMPRESSION RAMP: PRESSURE CONTOURS

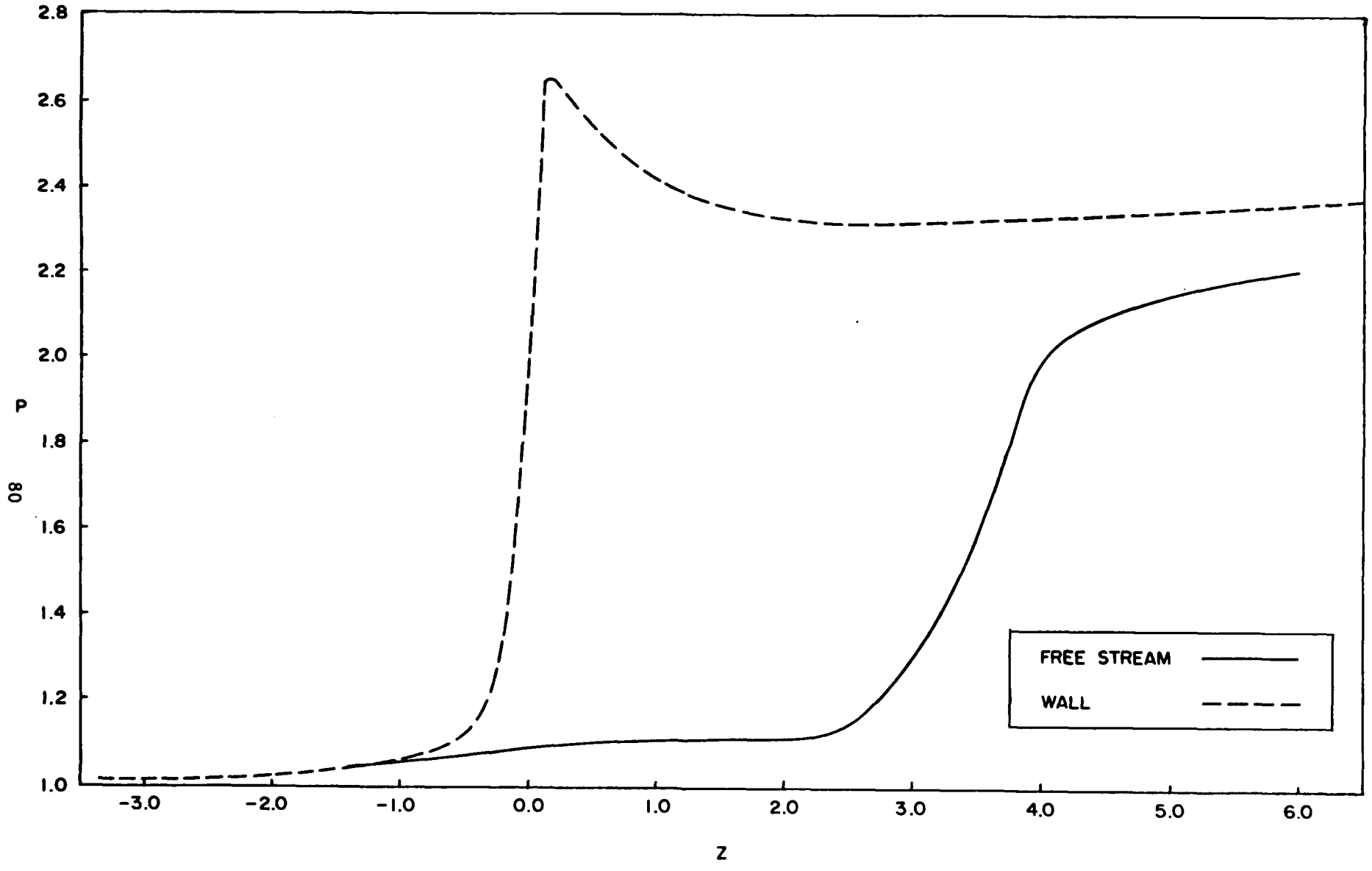


FIGURE 29 – STATIC PRESSURE DISTRIBUTION: AXISYMMETRIC COMPRESSION RAMP

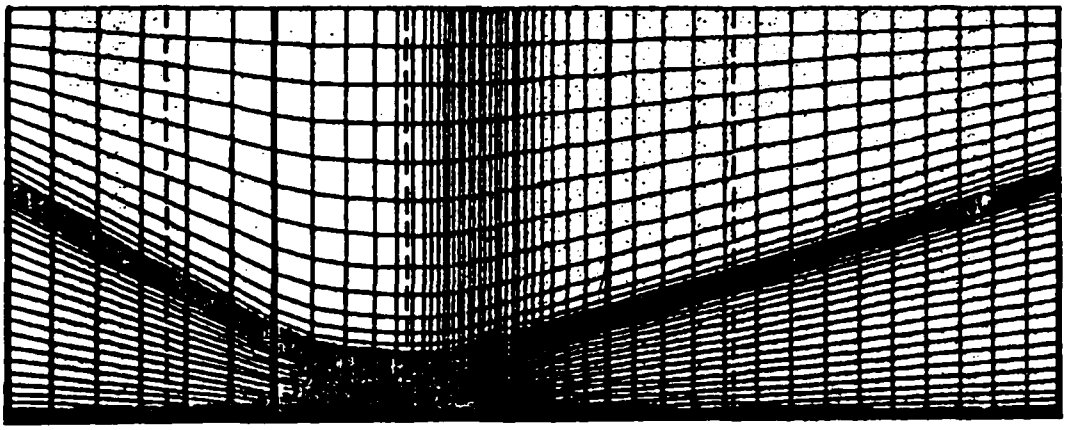

FIGURE 30 - COORDINATE SYSTEM FOR RESOLVING IMPINGING AND REFLECTED SHOCKS

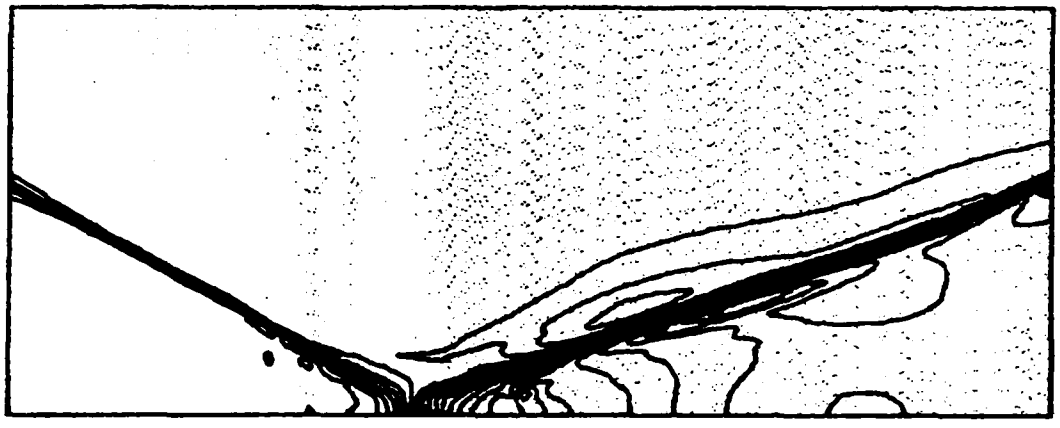

FIGURE 31- CONSTANT PRESSURE CONTOURS FOR SHOCK IMPINGING ON A TURBULENT BOUNDARY LAYER, USING SHOCK ADAPTING COORDINATE SYSTEM, M = 2.96, SHOCK GENERATOR ANGLE 10.89 DEGREES.

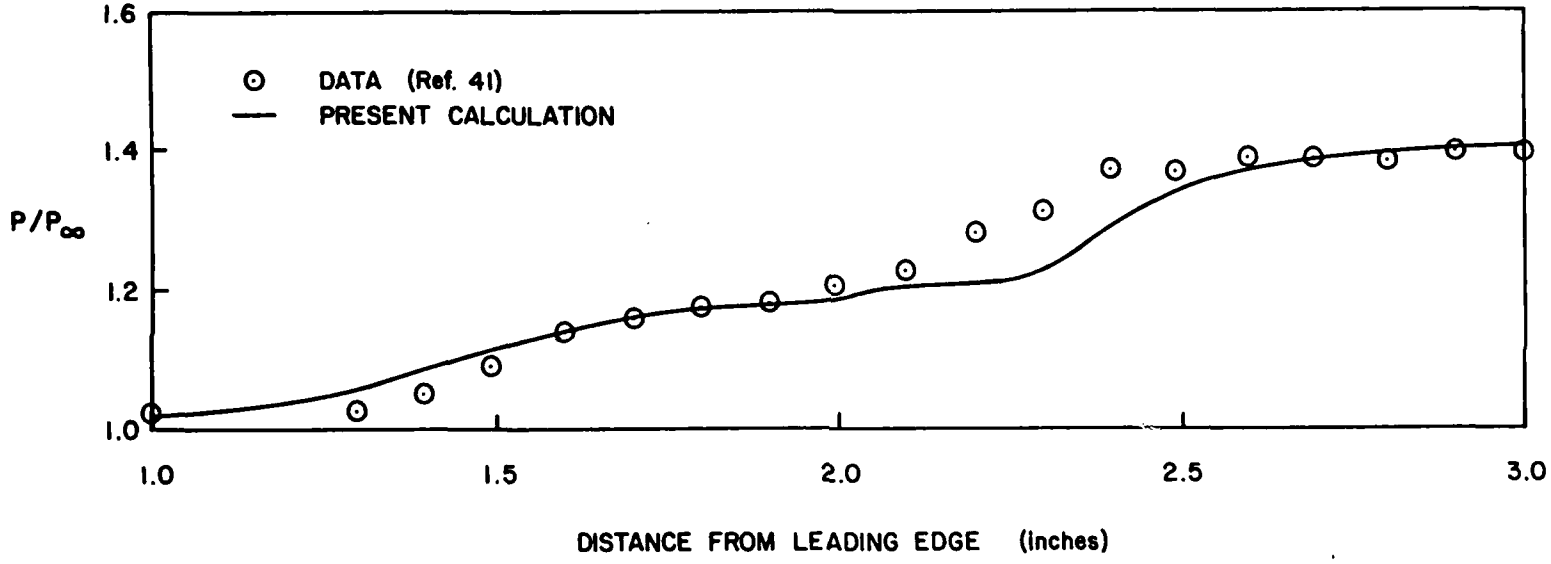


FIGURE 32 - WALL PRESSURE DISTRIBUTION FOR SHOCK WAVE IMPINGING ON A LAMINAR BOUNDARY LAYER; M = 2.0, INCIDENT SHOCK ANGLE 32.6 DEGREES.